Study on Synthesis and Characterization of Gadolinium Doped Cobalt Ferrites using Sol-gel Route

MS Theis

by

Sana Talib

CIIT/SP22-RPH-021/LHR

COMSATS University Islamabad

Pakistan

Fall 2023

Study on Synthesis and Characterization of Gadolinium Doped Cobalt Ferrites using Sol-gel Route

A Thesis Submitted to

COMSATS University Islamabad

In partial fulfillment

Of the requirement for degree of

Master of Science

in

Physics

by

Sana Talib

CIIT/SP22-RPH-021/LHR

Department of Physics

Faculty of Sciences

COMSATS University Islamabad

Pakistan

Fall 2023

Study on Synthesis and Characterization of Gadolinium Doped Cobalt Ferrites using Sol-gel Route

This thesis is submitted to the Department of Physics as partial fulfillment of the requirement of for the award of Degree of Master of Sciences in Physics.

Name	Registration Number
Sana Talib	CIIT/SP22-RPH-021/LHR

Supervisory Committee

Supervisor

Dr. Salman Naeem Khan
Associate Professor
Department of Physics
CUI, Lahore Campus
COMSATS University Islamabad,
Lahore Campus

Final Approval

Study on Synthesis and Characterization of Gadolinium Doped Cobalt Ferrites using Sol-gel Route

By

Sana Talib

CIIT/SP22-RPH-021/LHR

Has been approved

For the COMSATS University Islamabad, Lahore

External Examiner: _____

Dr. Masood Ul Hassan Farooq

Associate Professor, Department of Basic Sciences and Humanities, UET New Campus (KSK)

Supervisor: _____

Dr. Salman Naeem Khan

Associate Professor, Department of Physics, CUI, Lahore

Co-Supervisor: _____

Dr. Amna Mir

Assistant Professor, Department of Physics, CUI, Lahore

HOD: _____

Prof. Dr. Muhammad Ashfaq Ahmed

Head of Department Physics, CUI, Lahore

Author’s Declaration

I Sana Talib, CIIT/SP22-RPH-021/LHR hereby declare that I have produced this work, which is presented in this thesis, during the scheduled period of study. I also declare that I have not taken any material from any source except referred to wherever due to that amount of Plagiarism is within an acceptable rang. If a violation of HEC rules on research has occurred in this thesis, I shall be liable to punishable action under plagiarism rules of HEC.

Dated: _____

_____

Sana Talib

CIIT/SP22-RPH-021/LHR

Certificate

It is certified that Ms. Sana Talib CIIT/SP22-RPH-021/LHR has carried out all research work related to this thesis under my supervision at Department of Physics, COMSTAS University Islamabad (CUI), Lahore Campus and the work fulfills the requirement for the award of the degree of MS in Physics

Date: _____

Supervisor:

_____

Dr. Salman Naeem Khan
Associate Professor
Department of Physics
CUI, Lahore Campus

Dedication

As parents are the greatest blessing of ‘ALLAH ALMIGHTY’, they paid their full attention for our success in every field of life. Our beloved parents build our character towards hardworking, truthfulness, fair dealing, and humanity. They supported us in achieving the destination and help to go to the right way to find the goal for which we dreamed ever. Here a lot of favors made from my parent’s side in my doings throughout my carrier; even I have no words to narrate all the things made by them for me. Therefore, this passion and love for study is a result of their noble teaching. This research work and outputs, with my deepest gratitude and warmest affection dedicates to my beloved parents, brothers, and sisters. Their love and endless efforts help me to write this.

Acknowledgement

All Praises be to Allah, the Beneficent and the Merciful. I am highly thankful to Allah Almighty for giving me the wisdom, strength, courage and vision to complete this work.

I consider it an opportunity to express my deep and heartily thankfulness to my devoted Co-supervisor Dr Amna Mir, Assistant professor, Department of Physics, COMSATS university Islamabad, Lahore for his cooperation and for providing me with all necessary facilities.

I'd like to thank my supervisor, Dr. Salman Naeem Khan, Associate Professor, Department of Physics, COMSATS University Islamabad, Lahore Campus, for his expert supervision, constant encouragement, attention, and dedicated engagement in helping me improve and finish this research work. Without him, my research would have been incomplete.

Words are inadequate to express my humble obligation and gratitude to my Father Mr. Talib Hussain, my mother, and my siblings for their support, good wishes, inspirations, and unceasing prayers for me, without which my present destination would have remained a dream.

Sana Talib

CIIT/SP22-RPH-021/LHR

Abstract

Study on Synthesis and Characterization of Gadolinium Doped Cobalt Ferrites using Sol-gel Route

In this research work, Gadolinium doped cobalt ferrite ($CoFe_{2-x}Gd_xO_4$) nanoparticles were prepared by sol-gel auto-combustion method and their nano-composites with Multi-Walled Carbon Nanotubes (MWCNTs) were synthesized using ultra-sonication route. Gadolinium (Gd) is a rare earth element and it is very important in magnetic resonance techniques because of its strong paramagnetic properties. The nano-composites were characterized through UV-visible spectroscopy, Fourier Transform Infrared Spectroscopy (FTIR), scanning electron microscopy (SEM) and Energy Dispersive X-ray Analysis (EDX). Fourier transform infrared spectroscopy demonstrates the existence of functional groups on the surface of carbon nanotubes and the aggregation of Gd doped cobalt ferrites nanoparticles on MWCNTs was seen by SEM. The absorption and the optical band gaps values are showing increasing trend with increasing doping concentration and with CNTs deposition, which is also evidencing the enhancement of magnetic behavior. The research revealed that Gadolinium doping influenced the crystal structure, magnetic behavior, and electrical conductivity of cobalt ferrite. These changes can be utilized to tailor the properties of cobalt ferrite for specific applications like tunable dielectric devices, magnetic storages devices, and sensors.

Table of Contents

List of Figures

List of Tables

List of Symbols

μ	magnetic moment
e	charge of an electron
L	angular momentum of the electron
h	Planck's constant
S	spin quantum number
I	current
A	area vector
μ_s	spin magnetic moment
gs	Lande g-factor
μ_B	Bohr magneton
ms	electron spin quantum number
μ_l	orbital magnetic dipole moment
l	orbital quantum number
χ	magnetic susceptibility
H	magnetic field
M	magnetization
C	Curie constant
T_c	Curie temperature

Chapter 1

Introduction

1.1 Tracing Origin of Magnetism

Electrons move in orbit around the nucleus of an atom and spin on their own axis, which is cause of magnetism. The magnetism of a substance is determined by how strongly the magnetic moments of its constituent atoms interact with one another. There is no considerable connection between the atomic magnetic moments in few materials, but these moments highly related in others. Thus, magnetic moment of an electron in orbit [1] can be expressed

$$\mu = \frac{e^2 \times L}{2me} \tag{1}$$

Where:

- μ represents magnetic moment (Am^2)
- e represents charge of an electron ($1.602 \times 10^{-19}\ C$)
- L represents orbital angular momentum (Js)
- m represents mass of an electron ($9.109 \times 10^{-31}\ kg$)

The Bohr quantization condition [1] can be expressed mathematically as:

$$L = \frac{nh}{2\pi} \tag{2}$$

Where:

- L represents angular momentum of the electron (Js)
- n represents an integer (1, 2, 3, ...)
- h shown as Planck constant ($6.626 \times 10^{-34}\ Js$)

This means that an electron's rotational momentum can only take on discrete values given by the integer n. This is in contrast to classical mechanics, where the angular momentum of an object can take on any value.

An electromagnet is a basic device that uses electricity to generate a magnetic field. Wrapping a coil of wire around a core, such as an iron nail, creates it. When an electric current passes through the wire, it generates a magnetic field that aligns the iron atoms in the core, converting it into a temporary magnet. Because it is easily magnetic, iron is a common core material. Electromagnets are employed in a wide range of applications, including lifting large items, metal separation, and electricity generation. Each electron functions as a little magnet. It has a spin magnetic moment due to its spinning and its own orbital moment, which is expressed in Bohr magnetons (B). In most materials, there is no net magnetic moment because the magnetic moments of paired electrons cancel each other effect.

In certain magnetic materials, a significant number of electrons align their magnetic moments, creating an integrated magnetic field. This field, generated by the material or an electromagnet, has supervision and exerts a force on any magnet, attempting to line up with the external field. The lowest viable magnetic moment due to electron spin is $\mu = eh/4\pi m$. Quantum theory dictates that electron spins can only have two values: $(+1/2)$ or $(-1/2)$. The equation can be written as [2]:

$$\mu = \left(\frac{e}{2m}\right) S \tag{3}$$

Where:

- μ represents magnetic moment of the electron (Am^2)
- e known as charge of electron $(1.602 \times 10^{-19}\ C)$
- m known as mass of an electron $(9.109 \times 10^{-31}\ kg)$
- S represents spin quantum number $(1/2)$

This equation can also be written as:

$$\mu = g\left(\frac{e}{2m}\right) S \tag{4}$$

Where:

- g is known as Lande-factor

It's a dimensionless constant that depends on the specific atomic or molecular system [2]. For an electron, $g = 2.0023$. So, is short, the magnetic moment of an electron due to its spin is proportional to the spin quantum number S and is given by the equation $\mu = g(e/2m)S$. The spin subscription appears at $g = 2$ and the orbital contribution appears at $g = 1$. The nucleus has such a huge mass, the magnetic moment endowment can be ignored in comparison to the electronic magnetic moments. The gyromagnetic ratio is associated to the g-factor, and 'g' appears from electron precedency, which is analogous to the precession of a top in a gravitational attraction. The value of g indicates whether the magnetic moment is induced by electron or spin motion [2].

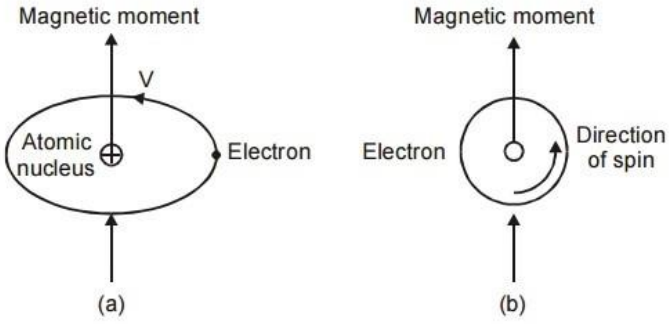

Fig 1.1: Magnetic moment of an electron (a) and spinning electron (b) [3]

1.1.1 Atomic Magnetic Dipole Moment

The dipole moment, or power, of a magnetic dipole reflects how well it can align itself with an outer magnetic field. The homogeneous magnetic field, the dipole moments magnitude is precisely proportional to the maximum torque that the dipole experiences when it is perpendicular to the magnetism. Field of magnets, commonly known as the magnetic dipole moment, is used to calculate the stability of a magnetic source [4]. The magnetic moment of simple current loop is calculated by using equation below:

$$\mu_m = \int I \, da \tag{5}$$

Where:

- μ_m represents magnetic moment (Am^2)

- I represents constant current flowing through the loop
- da represents vector area element of the loop

According to convention, the vector areas direction was determined by applying right hand rule. As you trace loop's current direction with your right hand, if your palm touches the loop's surface, your extended thumb will suggested the direction of the vector area.

The magnetic moment of a bar magnet can be understood by picturing it as a pair of magnetic pole of uniform intensity but reverse polarity. Every pole produces a magnetic force that diminishes with interspace. Because the magnetic poles are always in couple, their intensity interacts, resulting in a pulling force from one pole and a repelling force from the other. This involvement is most noticeable when the poles are adjacent together, as with short bar magnets. As a result, the magnetic force constructed by bar magnet at a particular place in extent is determined by two elements: the pole energy (P) and the distance (d) between them. The force created by bar magnet is directly proportional to the product of magnetic moment (μ) and the distance (R) between the magnet and the point where the force is being measured. The force of direction can be determined by the angle between the axis of a bar magnet and the distance vector.

The magnetic field can be generated using electrical current flowing through coils and loops. In a planar loop, the magnetic moment (μ) is equal to the product of the area (A) and the current (I) of loop. The relationship expressed by the formula given below:

$$\mu = IA \tag{6}$$

When the charged particle is in motion, it reveals a magnetic moment indistinguishable to that of a current loop. The magnitude of this magnetic moment calculate on the mass (m), particles charge (q), and velocity (v) [4]. This can be expressed mathematically as:

$$\mu = \frac{qmv \sin\theta}{2m} \tag{7}$$

Where: θ is angle between the magnetic field line and particles velocity vector.

The magnetic moment (μ_m) of a current-carrying loop can be calculated using the formula:

$$\mu_m = IA \tag{8}$$

Where:

- μ_m represents magnetic moment (Am^2)
- I represents current flowing through the loop, measured in amperes (A)
- A represents area vector of the loop, measured in square meters (m^2)

In layman's words, the magnetic moment of a current-carrying loop is proportional to both the current flowing through the loop and its area. The magnetic moments orientation is in opposition to the plane of the loop. Here's an illustration:

If a current of 2 A flows through a circular loop with an area of $0.1m^2$, then the magnetic moment of the loop would be:

$$\mu_m = (2\ A) \times (0.1\ m^2) = 0.2\ Am^2 \tag{9}$$

Therefore, the magnetic moment of the loop would be 0.2 ampere-square meters.

1.1.2 The Magnetic Moment of Electrons

The electron, a negatively charged particle with angular momentum, behaves like tiny bar magnet when placed in an electric field. This is due to its rotational motion, which creates a magnetic dipole effect. Like bar magnet, the electron has two poles of equal magnitude but different polarity; a magnetic south pole and a magnetic north pole. In magnetism, the electron experiences a torque that opposes its orientation with the field, resulting in potential energy that based on its alignment relative to the field**.** According to classical mechanics, an electron's magnetic energy is approximately twice that of its normal energy. This discrepancy is assigned to the fact that the electrons spin angular momentum is twice as effective in manufacturing a magnetic moment as considered to its orbital angular momentum. The factor is known as the electrons spin factor (g). Firstly, spectroscopists including A. Lande, developed method to evaluate the influence of numerous angular momentum directions on the electrons magnetic

moment. The resulting geometric factor is also referred as the g-factor of Lande. The elemental magnetic moment (μ) is given as [5]:

$$\mu = s\left(\frac{q}{2m}\right) g_{\mu} \tag{10}$$

Where:

- g_{μ} is a generalized variable quantity

The g-factor is an important parameter associated with the magnetic moment of sub-atomic particles that determines how much particles angular momentum is preferred, or how it processes in a magnetic field. One of the most impressive feats of quantum electrodynamics (QED) is to predict the electron g-factor, called "anomalous magnetic moment", which has experimentally been measured to be 2.002319. The source of 2 in the electrons g-factor is the Dirac equation, a fundamental equation of quantum mechanics that relates the electron spin to its electromagnetic properties. The remaining 0.002319 correction is known as the anomalous magnetic dipole moment (aEDM) of the electron, and it arises from the electron's interaction with virtual photons in quantum electrodynamics (QED). The Dirac equation itself when “quenched” or simplified for an electron in a magnetic field reduces down to the Schrödinger equation with an additional term. This additional term accounts for the interaction between the intrinsic magnetic moment of the electron and the magnetic field, and the value of this term in agreement provides the correct energy.

The equation for calculating the total spin magnetic moment of an electron is [6]:

$$\mu_s = \frac{(gs \times \mu_B \times s)}{2} \tag{11}$$

Where:

- μ_s represents spin magnetic moment (Am^2)
- gs represents Lande g-factor, which is approximately 2 for electrons
- μ_B represents Bohr magneton, equal to ($9.274 \times 10^{-24}\, Am^2$)
- ms represents electron spin quantum number, which is 1/2 for electrons

The electron magnetic moments z-component can be expressed as:

$$\mu_z = gs * \mu_B * ms \quad (12)$$

Where:

- μ_z represents the magnetic moment of z-component (Am^2)
- m represents spin quantum number projection, which can be $\pm 1/2$ for electrons

Total magnetic dipole moments caused by orbital angular momentum [6] are shown:

$$\mu_l = \mu_B \times \sqrt{l(l+1)} \quad (13)$$

Where:

- μ_l represents orbital magnetic dipole moment (Am^2)
- l represents orbital quantum number

The orbital magnetic dipole moment of z-component for an electron with a magnetic quantum number ml can be expressed:

$$\mu_{zl} = \mu_B * ml \quad (14)$$

Where:

- μ_{zl} represents the orbital magnetic dipole moment of z-component (Am^2)
- ml represents magnetic quantum number projection, which ranges from -l to l

The total magnetic moment of an electron is the product of its orbital magnetic dipole moment and spin magnetic moment. The spin magnetic moment is a fundamental feature of the electron. The orbital magnetic dipole moment can determined by the orbital quantum number of the electron.

1.2 Magnetic Behavior

The magnetic properties are caused principally by electrons in atoms, which have a magnetic moment due to their mobility. This motion can have two forms: spin motion and orbital motion. Each type of motion contributes to the magnetism of an electron. The magnetic induction or flux

density (B) of a material and the influence it has on the magnetic induction within the material, represented by magnetization (M), characterize its reaction to an external magnetic field (H). A fundamental relationship between these three magnetic quantities is expressed by the equation [1]:

$$B = \mu_0(H + M) \tag{15}$$

Where:

- μ_0 is constant of permeability in free space
- μ represents the permeability of the material

Equation (14) separates the magnetic induction generated solely by the field $(\mu_0 H)$ from the magnetic induction subscribed by the material $(\mu_0 M)$.

The susceptibility (χ) [5] can described the ratio of magnetization to the applied magnetic field H:

$$\frac{M}{H} = \chi \tag{16}$$

The equation connects a material's permeability and susceptibility:

$$\mu = \mu_0(1 + \chi) \tag{17}$$

1.2.1 Types of magnetic behavior

Following are major types of magnetic behavior of materials:

Diamagnetism: Diamagnetism is an inherent feature of all materials, however hardly manifested. In the presence of an external magnetic field, it is brought on by the non-cooperative behavior of circling electrons. Diamagnetism substances made up of atoms that have no magnetic moments, suggesting that all electron orbitals filled and have no unpaired electrons exist. When revealed to a magnetic field, however, negative magnetization is induced, resulting in a negative susceptibility. This behavior is consistent with Lenz's law. Temperature-

independent susceptibility is another feature of diamagnetic materials. Typical susceptibility values range from $10^{-6}\ to\ 10^{-5}$. Numerous materials, including B, S, Cu, N_2, and the majority of organic molecules, are diamagnetic [6].

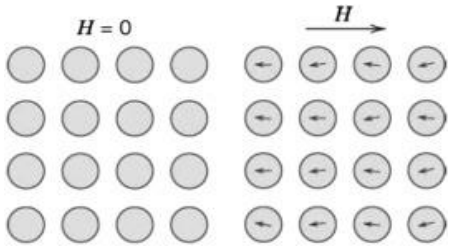

Fig 1.2: Diamagnetic Materials [7]

Para-magnetism: Because of the imperfect cancellation of orbital magnetic moments (unpaired electrons) or electron spin, paramagnetic materials have a persistent magnetic dipole moment. These dipole moments are orientated randomly in the absence of an external magnetic field, resulting in no net macroscopic magnetization for the material. When an external magnetic field is applied, these dipole moments tend to align themselves by rotating in the direction of the applied field, resulting in net magnetization of the material. Magnetic moments can be aligned along an applied field, resulting in positive susceptibility [8]. The values of susceptibility for paramagnetic materials are very small, range from $10^{-5} - 10^{-3}$. Curie's law states that the susceptibility of a paramagnetic material is inversely proportional to temperature [1]:

$$\chi = \frac{C}{T} \tag{18}$$

Where:

- C is the Curie constant.

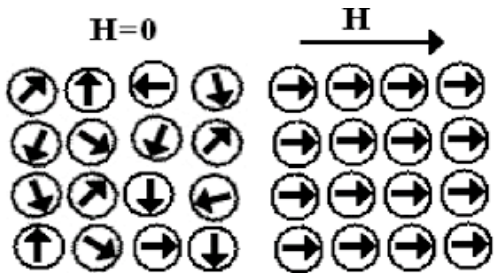

Fig 1.3: Paramagnetic Materials [9]

Ferromagnetism: In various ways, ferromagnetic materials differ greatly from diamagnetic and paramagnetic materials. The exchange coupling between neighboring magnetic moments in a ferromagnetic material enables them to align parallel with each other. This permanent magnetic moment results from the cooperative interaction of many atomic spins within domains, which are places where all spins are aligned in the same direction. The exchange force is a quantum mechanical phenomena that is determined by the relative orientation of two electron spins. Because all magnetic moments easily align together, ferromagnetic materials can generally develop a significant magnetization even in the absence of an external magnetic field. A ferromagnetic material's susceptibility does not follow Curie's law, but rather exhibits a modified behavior characterized by the Curie-Weiss law:

$$\chi = \frac{C}{T - \theta} \tag{19}$$

Where:

- C is a constant
- θ is called the Weiss constant

The Weiss constant is nearly equivalent to the Curie temperature (T_c) for ferromagnetic materials. Magnetic moments are ordered at temperatures below T_c, but at temperatures beyond Tc, the material loses its magnetic ordering and exhibits paramagnetic behavior. [10]. $Fe, Co, Ni,$ and several of their alloys are examples of ferromagnetic materials. Ferromagnetic materials have two unique properties.

Spontaneous magnetization: In the absence of a field, this is the net magnetization that exists within an evenly magnetized microscopic volume. The magnitude of this magnetization, Ms, is determined by electron spin magnetic moments.

A magnetic ordering temperature (Curie temperature) exists**:** At the Curie temperature, spontaneous magnetization is zero. The Curie temperature is an intrinsic characteristic as well.

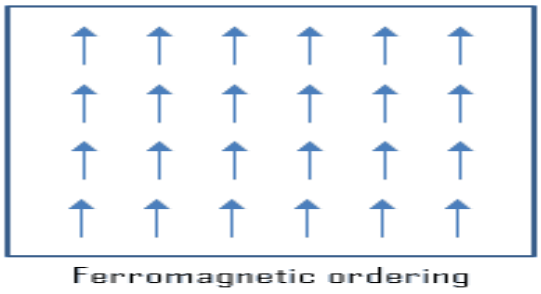

Fig 1.4: Ferromagnetic Material [11]

Antiferromagnetism: The magnetic moments of nearby atoms align antiparallel in antiferromagnetic materials, resulting in a net magnetic moment of zero. This indicates that the individual magnetic moments cancel out, and the material has no overall magnetism [12]. As shown in equation, the susceptibility of antiferromagnetic materials follows the Curie-Weiss law with a negative value of Fig 1.5 depicts the inverse susceptibility as a function of temperature. $MnO, FeO, CoO,$ and NiO are examples of antiferromagnetic materials.

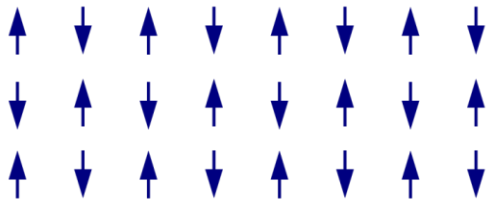

Fig 1.5: Anti-Ferromagnetic materials [13]

Ferrimagnetism: Ferrimagnetic materials and antiferromagnetic materials have the same antiparallel alignment of magnetic moments. However, the amplitude of the magnetic moment in one direction differs from that in the opposite direction in ferrimagnetic materials. Even in the absence of an external magnetic field, this discrepancy results in a net magnetic moment [14]. The susceptibility behavior of ferrimagnetic materials follows the Curie-Weiss equation and has a negative. Because of the crystal structure of ionic substances, particularly oxides, more sophisticated kinds of magnetic ordering can occur. Two magnetic sublattices (designated A and B) are separated by oxygen atoms in the magnetic structure. The exchange interactions take place via the oxygen anions. In this case, the exchanges are referred to as indirect or super-exchange interactions. The greatest super-exchange interactions result in spins aligning

antiparallel between the A and B sublattices. The magnetic moments of the A and B sublattices are uneven in ferrimagnets, resulting in a net magnetic moment. As a result, ferrimagnetism is similar to ferromagnetism. It demonstrates all of the characteristics of ferromagnetic behavior, including spontaneously magnetization, Neel temperature, hysteresis, and remanence. However, the magnetic ordering of ferro- and ferrimagnets is considerably different.

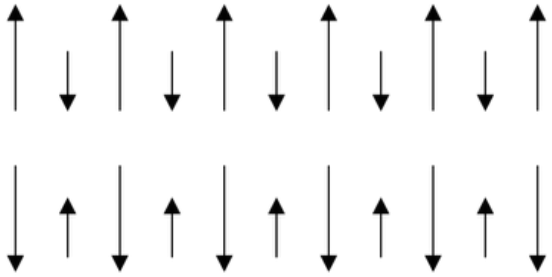

Fig 1.6: Ferrimagnetic Materials [15].

1.3 Ferrites

Ferrites are a significant class of materials with distinct properties and phenomena that can be exploited in a wide range of scientific and technological applications. Ferrites are used in many different sectors, including electronics, electro mechanics, magnetics, magneto-electronics, electrochemical science and technology, and biotechnology [16]. Spinel structured ferrite materials offer exceptional characteristics that make them ideal for sensor as well as transducer applications. Some of the important properties that allow such materials to be integrated into solid state electronics and magneto-electronics are high saturation magnetization, high-frequency high permeability, and very high electrical resistivity. The standard chemical formula for ferrites is B_2O_4 , where A is a divalent metal such as Mg^{2+}, Ni^{2+}, Co^{2+}, Zn^{2+}, or Cd^{2+} and B represents the trivalent metals such as Iron, aluminum, chromium and manganese. Typically, ferrite is magnetite (Fe_3O_4), which has been known as magnetic oxide since ancient times. Magnetite is a type of ferrimagnetic mineral that exists among the tetrahedral A and octahedral B sites. There are 64 tetrahedral and 32 octahedral spaces available for cations in one unit cell of ferrite, of which only 8 tetrahedral as well as 24 octahedral are occupied by cations.

1.3.1 Classification of ferrites

There are three main types of ferrites:

- Spinel Ferrites
- Hexagonal Ferrites
- Garnets

1.3.1.1 Spinel ferrites

The most common ferrite family is spinel ferrites, commonly known as cubic ferrites. Their high electrical resistivity and minimal eddy current losses make them ideal for microwave applications. Bragg and Nishikawa discovered the spinel structure of ferrites in 1915 [17][18], as represented by the mineral spinel $MgAl_2O_4$. A spinel ferrite has the typical chemical formula MFe_2O_4, where M represents a divalent metal ion such as Mg^{2+}, Ni^{2+}, Co^{2+}, Zn^{2+},or Cd^{2+}or a combination of these ions. Spinel ferrites possess a face-centered cubic (FCC) unit cell that accommodates eight formula units. The formula can be represented as $M_8Fe_{16}O_{32}$. The majority of the unit cell is made up of anions, which form an FCC lattice. There are two types of interstitial places in this lattice: tetrahedral (A) sites and octahedral (B) sites. Metallic cations occupy these locations. The unit cell has 96 interstitial sites, 64 of which are tetrahedral (A) and 32 of which are octahedral (B).

Tetrahedral Sites: The tetrahedral (A) sites in spinel ferrites are positioned in the middle of a tetrahedron produced by four lattice atoms. Three of these anions are in a plane, while the fourth is above the middle of the three. The cation fills the space left by these four anions. To ensure charge neutrality, cations occupy just 8 of the 64 tetrahedral (A) sites in the FCC crystal structure.

Octahedral Sites: Spinel ferrites have octahedral (B) sites in the core of an octahedron made up of six lattice anions. Four of these anions are in a plane, while the other two are symmetrically above and below the plane formed by the four anions. The cation occupies the gap left by the six anions, generating an octahedral structure. Cations occupy 16 of the 32 octahedral (B) sites in a spinel structure to preserve charge neutrality. Each unit cell in the FCC crystal structure has four octahedral sites. Figure 1.7 displays the octahedral site within an FCC lattice.

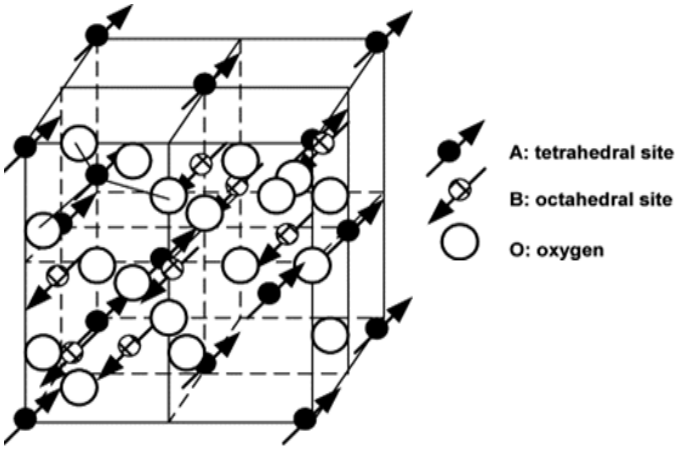

Fig 1.7: Structure of Spinel Ferrites [19]

1.3.1.2 Categories of spinel ferrites

The distribution of cations on tetrahedral (A) and octahedral (B) sites divides spinel ferrites into three groups.

- **Normal spinel ferrites**

All divalent metal cations (Me^{2+}) occupy the tetrahedral (A) sites in normal spinel ferrites, whereas all trivalent iron cations (Fe^{3+}) occupy the octahedral (B) sites. The structural formula for these ferrites is represented as (Me^{2+})[Fe^{3+}] O_4^{2-}. Zinc ferrites exhibit this type of distribution represented by the structural formula (Zn^{2+})[Fe_4^{3+}] O_4^{2-}.

- **Inverse spinel ferrites**

Inverse spinel ferrites are characterized by the exclusive presence of divalent metal cations (Me^{2+}) at octahedral (B) sites. Trivalent iron cations (Fe^{3+}) are dispersed evenly among both tetrahedral (A) and octahedral (B) sites. These structural formulae are of the form, Fe^{3+} [Me^{2+} Fe^{3+}] O_4^{2-}. Magnetite (Fe_3O_4), nickel ferrite ($NiFe_2O_4$), and cobalt ferrite ($CoFe_2O_4$) are examples of inverse spinel ferrites. Half of the Fe^{3+} ions in inverse ferrites dwell at A-sites, whereas the other half reside at B-sites. Their magnetic moments cancel each other out, and the ferrite's magnetic moment is derived from the magnetic moments of bivalent cations (Me^{2+}) in the B-positions.

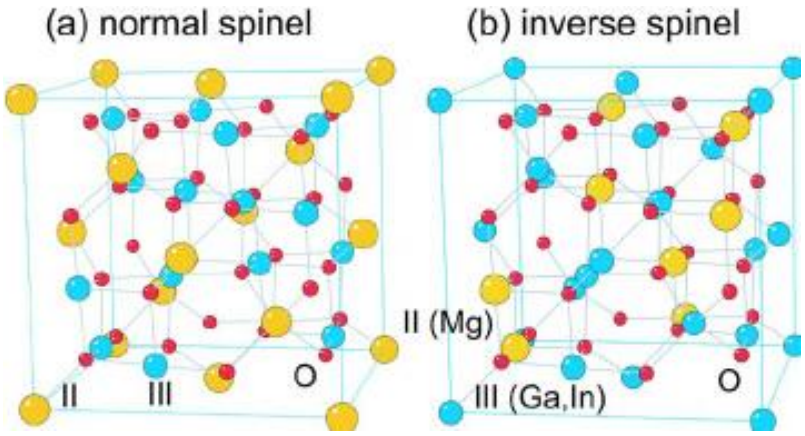

Fig 1.8: Normal Spinel and Inverse Spinel Ferrites [20]

- **Mixed Spinel ferrites**

Mixed spinel ferrites belong to an attractive class of materials that have a cubic crystal structure made of oxygen, iron, and other metal ions. Consider an oxygen atom grid with two unique "slots" for metal ions: tetrahedral (surrounded by four oxygen ions) and octahedral (surrounded by six oxygen ions). These spaces are occupied by a mixture of iron (Fe^{3+}) and other metal ions (Me^{2+}) such as zinc, magnesium, or cobalt.

1.3.1.3 Hexagonal ferrites

Gorter, Went, and Rathenau, and Van Oostershout discovered hexaferrites in 1952, followed by Wijn, Jonker, and Braun in 1956. These ferromagnetic oxides have a hexagonal or rhombohedral crystal structure with the formula $MFe_{12}O_{19}$, where M might represent elements such as barium, lead, or strontium. The oxygen ions in these ferrites form a hexagonal crystal structure that is densely packed. Because of their strong coercivity, hexaferrites are commonly employed as permanent magnets and are particularly well suited for applications at very high frequencies. Their hexagonal ferrite lattice matches the spinel structure with tightly arranged oxygen ions, but some layers include extra metal ions with ionic radii similar to oxygen ions. Hexaferrites, as opposed to garnet ferrites, may accommodate bigger ions, primarily barium, strontium, or lead, which are added by replacing oxygen ions.

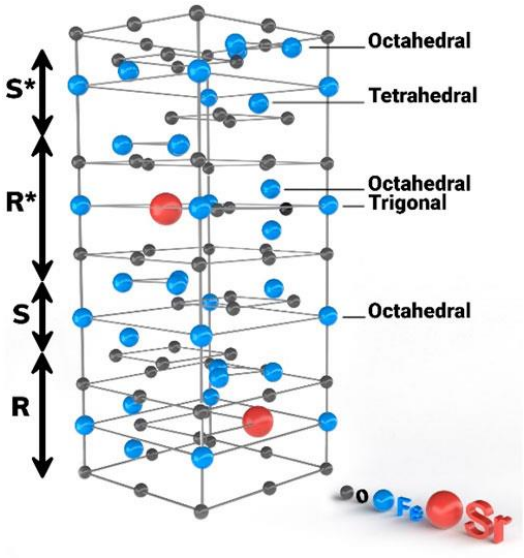

Fig 1.9: Hexagonal Ferrites [21]

1.3.1.4 Garnets Ferrites

In 1951, Yoder and Keith demonstrated that Substitutions in the ideal mineral garnet could be made $Mn_3Al_2Si_3O_{12}$. By replacing MnII+SiIV with YIII+AlIII, they produced the first silicon-free garnet, $Y_3Al_5O_{12}$. Bertaut and Forret followed suit in 1956 by synthesizing $Y_3Fe_5O_{12}$ and characterizing its magnetic properties. Geller and Gilleo further expanded the field in 1957 by preparing and studying $Gd_3Fe_5O_{12}$, another ferromagnetic compound. Pure iron garnets have the general formula $M_3Fe_5O_{12}$. Their unit cell is cubic, with roughly 12.5 edge length. Garnets are highly appreciated for their function in memory storage systems, despite their complicated crystal structure.

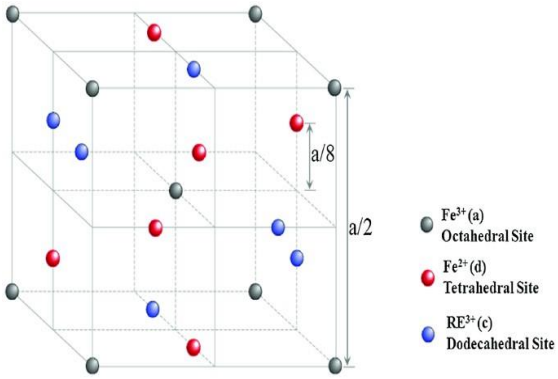

Fig 1.10: Garnet Ferrites [22]

1.3.2 Ferrites Magnetization

Hard ferrites and soft ferrites determined by their response to external magnetic fields. Soft ferrites can be magnetized as well as demagnetized easily, while hard ferrites are resistant to magnetization and demagnetization.

- **Soft ferrites**

  The low coercive force and strong magnetization of soft ferrites distinguish them, making them easy to magnetize and demagnetize. These properties are essential for applications in transformers, Microwave devices, inductors, as well as recording heads. These ferrites exhibit a thin and long hysteresis loop, indicating minimal energy loss during magnetization and demagnetization cycles. Examples of soft ferrites include nickel, iron, cobalt, and manganese [22].

- **Hard ferrites**

  Soft and hard ferrites are both difficult to magnetize as well as demagnetize. Due to their high coercive force and wide hysteresis loop. These properties make them suitable for permanent magnet applications. Examples of hard ferrites include alnico and rare-earth metal alloys. The introduction of hard ferrites in the 1950s marked a significant advancement in the development of permanent magnets. These ferrimagnetic materials possess relatively low remanence (approximately $400\,mT$) but remarkably high coercivity (approximately $250\,kA/m$), far exceeding other magnetic materials. While their maximum energy product is only around $40\,kJ/m^3$, hard ferrites can effectively moderate demagnetizing fields, making them valuable for applications such as permanent magnet motors. Therefore, permanent magnets, loudspeakers, DC magnets, and other devices are made from hard ferrites [23].

1.4 Rare Earth Elements

Rare earth elements (RE) include the complete lanthanoid series (atomic numbers 57 to 71), scandium (Sc 21), and yttrium (Y 39) [24]. Because of their comparable ionic radii and proclivity to dwell within the same ore deposits, these elements are frequently classified together. The term "RE" refers to the dispersed nature of these elements, which

occur in modest concentrations inside diverse minerals.RE elements have comparable chemical properties [25], which are distinguished by their strong electro-positivity and predominance in the trivalent state (although some lanthanoids can adopt other oxidation states). The radii of trivalent lanthanoid ions continuously shrink with increasing atomic number, resulting in lanthanoid contraction [26]. This contraction, in conjunction with the successive filling of the shielded 4f-orbital from cerium (Ce 58) to lutetium (Lu 71), forms the basis for the distinct electrical, optical, and magnetic properties exhibited in RE elements [27].

The unique electronic configurations of RE elements lead to a diverse range of properties, including:

- 4f orbital interactions: The 4f electrons in RE elements can interact with each other, giving rise to magnetic properties, such as paramagnetism, ferromagnetism, and antiferromagnetism.

- The ability of the 4f electrons to absorb and emit light leads to the distinct luminescent properties of the RE elements that are exploited in various applications, including as laser materials and phosphors for fluorescent lighting [28].
- The capacity of the RE elements to form strong bonds with a variety of elements renders them effective catalysts for wide range of chemical reactions.
- RE elements display a wide range of oxidation states, so that they are able to act as electron donors or acceptors, contributing further to their redox properties.
- The unique properties of the RE elements have seen a huge variety of applications in a range of fields including the following:
- Electronics: RE elements are employed in the production of magnets, semiconductors and in high- performance capacitors [29].

- Energy: RE elements are crucial components in batteries, fuel cells, and energy-efficient lighting systems [30].

- Environmental technologies: RE elements are used in catalytic converters to reduce harmful emissions and in water purification systems [31].
- Medical applications: RE-based contrast agents enhance the clarity of MRI scans, and RE compounds are used in cancer treatment and drug delivery [32].

RE elements play an increasingly significant role in modern technology and are essential for various emerging applications. As research and development continue, the potential of RE elements is likely to expand further, leading to groundbreaking advancements in various fields**.**

1.5 Gadolinium

Gadolinium (Gd) is a silvery-white rare earth metal that belongs to the lanthanide family. Gd Crystallizes in a hexagonal close-packed form and has an atom weight of $157.25\ g/mol$. The structure changes to a body-centered cubic structure when heated [33]. Because Gd possesses seven unpaired electrons in the f-shell, it has good magnetic characteristics, i.e. it is paramagnetic. With the exception of Xenon-135, Gd has the largest thermal neutron capture cross-section. Gd is employed as a positive contrast agent in T1 weighted imaging because of its paramagnetic characteristic. The chemical formula for gadolinium oxide is Gd_2O_3. It has a cubic crystal structure and appears as a white powder with a small tendency to absorb moisture (hygroscopic). Gadolinium oxide has a density of $7.07\ g/cm^3$ and a molecular weight of $362.50\ g/mol$. It also has a molar magnetic susceptibility, abbreviated as m, of $53.2\ x\ 10^{-3}\ cm^3$ [25].

Chapter 2

Literature Review

H. Nikmanesh et al. 2022 synthesized Samarium-doped cobalt ferrite nanoparticles using the method called Sol-gel route. Properties like crystal structure, morphology, and magnetic were investigated, confirming in the cobalt ferrite lattice, successful substitution of Fe^{3+} by Sm^{3+} cation. FESEM and FTIR analysis was used to confirm the formation of nano-sized spinel ferrites. The saturation magnetization decreased with increasing Samarium content at room temperature but showed weaker decrease at 10K. When the temperature was reduced from 300 to $10K$, the saturation magnetization and coercive field increased significantly. The coercivity of this sample with $x = 0.06$ at $10K$ was significantly higher than at room temperature. The making of Samarium doped cobalt ferrite is a useful for average permanent magnets and high-density information storage at low temperatures [34].

M. S. I. Sarker et al. 2022 purposed the Gd-doped $CoFe_2O_4$ nanoparticles with varying Gd^{3+} content ($0.00\ to\ 0.15$) were synthesized using sol-gel method. These nanoparticles are in well-dispersed particles with an average size of $30\ nm$ according to TEM images, and FCC inverse spinel structure, magnetic measurements showed varying coercivity. $CoFe_{2-x}Gd_xO_4$ magnetic nanoparticles with 0.03% Gd^{3+} content exhibit high coercivity and magnetic anisotropy, making them potential candidates for data processing, automotive, and telecommunications applications [35].

S. B Das et al. 2022 exhibited spinel ferrite nanomaterial popularity has increased due to their applications in energy storage, electronic devices, and environmental monitoring devices. Yttrium-substituted $CoFe_{2-x}Y_xO_4$ nanomaterial was synthesized and their properties were analyzed. Cubic phase was confirmed by XRD analysis and showing a decrement in crystallite size value and lattice constant with increasing Y^{3+} content. The Rietveld refinements showed good fit ranges between 1.02 and 1.32, and analysis of surface morphology of $CoFe_2O_4$ and $CoFe_{1.7}Y_{0.3}O_4$ samples indicated agglomerated and porous structures with average grain sizes of 1.24 and 2.50μm, respectively. While HRTEM confirmed particle sizes of 30.40 and 10.92 nm for $CoFe_{2-x}Y_xO_4$ ($x = 0.0$ and 0.3). The addition of Y^{3+}in $CoFe_{2-x}Y_xO_4$ materials causes a slight shift in FTIR spectroscopy and an increase in direct band gap, while room temperature PL emissions indicate the presence of defects and vacancies. The decrease in magnetic properties suggests potential usage in magnetic hyperthermia. Thus ferroelectric properties of $CoFe_{2-x}Y_xO_4$ nanomaterial's, including their structural, optical, magnetic, and ferroelectric

properties, make them potentially useful in various applications such as photocatalysis, magnetism, opto-electronics, and the environment [36].

A. Rajeshwari et al. 2023 proposed Gd^{3+} doped manganese nano ferrites were synthesized using the Sol-Gel method route. The XRD resulting smaller crystallite size and spherical morphology with reduced agglomeration, and the dopant influenced the band gap. Gd^{3+}co-doping in manganese nano ferrites increased coercivity and decreased saturation, resulting in improved dielectric characteristics with increasing Gd^{3+} concentration and AC frequency, showing the lowest dielectric loss and highest dielectric constant [37].

A. A khan et al. 2022 explained the Yttrium-doped Copper ferrites are synthesized using the method called sol-gel auto-combustion technique. Their structural and morphological properties of the prepared samples are studied using XRD and SEM. The XRD results indicate the successful formation of stable tetragonal copper ferrite both with and without yttrium doping. By subjecting the samples to high sintering temperatures, successfully achieved a transformation to a tetragonal crystal structure. Raman and FTIR spectra used to analyze the vibrational modes, confirming the formation of a tetragonal structure with M-O bonding. The electromagnetic response of the powdered samples was studied in the microwave region from $(1\ to\ 15\ GHz)$. They observed a decrease in both real permittivity (from $5\ to\ 3\ F/m$) and real permeability (from $2.5\ to\ 1.75\ H/m$) as the Y^{3+}content increased. This trend was found to be directly related to the degree of crystallinity. Furthermore, the samples exhibited low values of dielectric and magnetic loss tangent, which makes these samples highly useful for applications where minimizing energy loss is essential [38].

S. Bajaj et al. 2023 explained the focuses on the synthesis process of In^{3+}doped cobalt ferrite ($CoFe_{2-x}In_xO_4$), where ($x = 0.00, 0.02, 0.04, 0.06, 0.08,$ and 0.10) at low temperatures by using the method called sol-gel auto-combustion. The samples obtained were thoroughly analyzed for their crystal structure and phase purity using XRD. Their results confirm single-phase cubic spinel structure's formation. The typical samples exhibit spherical grain formation with an average grain size of 36 nm, as observed in the FE-SEM images. The particle size, determined from the TEM histogram, ranges from $35\ to\ 32\ nm$. At Room temperature M-H plot indicates a decrement in saturation magnetization curve with doping, attributed to the reduction

in A-B interaction. Their real and imaginary parts of the dielectric constant show an exponential variation with frequency. Additionally, In^{3+}doping results in decrement of dielectric constant [39].

S. Sarmah et al. 2023 exhibited the study reports on the comprehensive investigation of polycrystalline material samples of $Co_{2-x}Fe_2Mg_xO_4$, where x ranges from 0.00 to 0.30, synthesized via the sol-gel process. The structural analysis, conducted through Rietveld refinement of analysis XRD patterns, confirms the formation of single-phase samples. Raman analysis reveals the presence of additional peaks at $620\ cm^{-1}$ and $660\ cm^{-1}$, indicating their mixed-spinel structure. With increasing Mg^{3+} substitution, the saturation magnetization decreases while there is an increase in coercive field initially. The impedance spectroscopy shows two relaxation peaks except for the $x = 0.30$ sample. The contribution of electro active regions is identified. Dielectric constants initially increase and then decrease the small polaron hopping is responsible for electrical conductivity [40].

A. A Al. Junaid et al. 2023 explained Lanthanum substitution in cobalt ferrites affects their structural, magnetic, and electrical properties. XRD and FTIR measurements show that La-substitution did not significantly affect size of crystal structure, but the formation of orthorhombic $LaFeO_3$ occurs at higher La-content. The magnetization decreases gradually as the La-content increases due to a decrease in super-exchange interaction, while the formation of antiferromagnetic leads to a significant reduction in magnetization. All samples exhibit hard magnetic characteristics and semiconducting behavior with decreasing electrical conductivity as La-content increases. The $LaFeO_3$ highlighted text suggests that the decrease in electrical properties in the material is because of the preferential occupation of La^{3+} by octahedral positions. The occurrence of electrical inhomogeneity caused by O_2 vacancy or the Maxwell-Wagner mechanism [41].

R. A Reddt et al. 2023 proposed Gadolinium-doped cobalt ferrite nano-powder samples were synthesized using a combustion method. FTIR and XRD results in single spinel phase formation. The doping of Gd^{3+} ions in the nano-powders reduced magnetization and increased coercivity. While the lattice constant increased and the average crystallite size value decreased with

increasing Gd^{3+} concentration. It was also significantly improving antimicrobial activity against various pathogens [42].

X. Jing et al. 2023 were synthesized nanoparticles called rare earth doped cobalt ferrite and the effect of replacing Co^{2+} or Fe^{3+} with RE^{3+} on their structure and magnetism properties of the nanoparticles was studied. Replacement of RE^{3+} ions by Co^{2+} ions yielded larger lattice distortion and smaller grains. In cobalt ferrite NPs, addition of 2+ ions decreased grain size and improved grain distribution and modified the magnetic properties (reduction in the saturation magnetization curve and the changes of the coercivity according to the 2+ and the site of these ions). Addition of Co^{2+} ions in cobalt ferrite increases coercivity, while substitution of RE^{3+} ions by Co^{2+} decreases it. This is due to cation rearrangement and variations in grain size, which control the magnetic domain structure, offers potential to enhanced coercivity in such materials [43].

D. T. Rahardjo et al. 2023 prepared Cobalt ferrite doped with yttrium. The crystal sizes and properties because of magnetic behavior of yttrium-doped cobalt ferrite nanoparticles were measured, showing a decrement in crystal size and magnetization saturation curve with increasing yttrium doping concentration. The Fourier Transform Infra-Red (FTIR) test revealed typical absorption curves at specific wave numbers [44].

Chapter 3

Research Methodology

And

Characterization Techniques

3.1 Sample Preparation Techniques

Synthesis is accomplished using a variety of approaches. The researcher chose them based on their benefits and shortcomings. But altering the synthesis type drastically alters the result [45].

- Hydrothermal method
- Co-Precipitation technique
- Sol-gel technique
- Solution combustion technique
- Spray pyrolysis
- Microwave technology and micro-emulsion technique

In this study endeavor, synthesis is accomplished using the Sol-gel, which has many advantages.

3.2 Sol Gel

The sol-gel process is a wet-chemical technique that is typically used to deposit nanocomposite films. A chemical procedure called the sol-gel method is used to create materials that resemble gel. This technique is widely used for the synthesis of different nanomaterials, thin films, and coatings as well as for the creation of ceramics and glasses. The term "gel" describes a 3D network of solid particles that has taken on the shape of the liquid in which it is distributed, whereas the term "sol" refers to a stable colloidal suspension of nanoparticles in a liquid [46].

3.2.1 Advantages of Sol Gel technique

The following are some benefits of sol-gel methods:
High purity multicomponent films can be prepared with great success using the sol-gel process. The sol-gel method has been used to create a variety of nanocomposite films that are utilized as the active ingredients in gas sensors.
An effective and economical substitute for traditional methods for producing nanocrystalline elemental, alloy, and composite powders is sol-gel synthesis [47].

3.3 Compositions for the samples Preparation

The chemical composition of the materials is

- $\boldsymbol{CoFe_2O_4}$ and $\boldsymbol{MWCNTs/CoFe_2O_4}$
- $\boldsymbol{5\%Gd/CoFe_2O_4}$
- $\boldsymbol{10\%Gd/CoFe_2O_4}$ and $\boldsymbol{MWCNTs/CoFe_{1.90}\ Gd_{0.10}O_4}$
- $\boldsymbol{15\%Gd/CoFe_2O_4}$
- $\boldsymbol{20\%Gd/CoFe_2O_4}$ and $\boldsymbol{MWCNTs/CoFe_{1.80}\ Gd_{0.20}O_4}$

3.4 Measurement of Chemicals for Samples Preparations

The measurements of $\boldsymbol{Gd}$ doped cobalt ferrite ($\boldsymbol{CoFe_{2-x}Gd_xO_4}$) are shown in table 3.1**.**

Table 3.1: Measurement of chemicals.

Sample no.	Composition	Chemicals	Quantity	Chemical Formula
1.	0.0	$Co(NO_3)_2.6H_2O$ $Fe(NO_3)_3.9H_2O$ $C_6H_8O_7$	2.18g 6g 4.56g	$CoFe_2O_4$
2.	0.05	$Co(NO_3)_2.6H_2O$ $Fe(NO_3)_3.9H_2O$ $Gd(NO_3)_3.6H_2O$ $C_6H_8O_7$	2.21g 6g 0.16g 4.68g	$CoFe_{1.95}\ Gd_{0.05}O_4$
3.	0.10	$Co(NO_3)_2.6H_2O$ $Fe(NO_3)_3.9H_2O$ $Gd(NO_3)_3.6H_2O$ $C_6H_8O_7$	2.27g 6g 0.34g 4.80g	$CoFe_{1.90}\ Gd_{0.10}O_4$
4.	0.15	$Co(NO_3)_2.6H_2O$ $Fe(NO_3)_3.9H_2O$ $Gd(NO_3)_3.6H_2O$ $C_6H_8O_7$	2.33g 6g 0.54g 4.92g	$CoFe_{1.85}\ Gd_{0.15}O_4$

5.	0.20	$Co(NO_3)_2.6H_2O$ $Fe(NO_3)_3.9H_2O$ $Gd(NO_3)_3.6H_2O$ $C_6H_8O_7$	2.39g 6g 0.74g 5.07g	$CoFe_{1.80}\,Gd_{0.20}O_4$

Chemical equation is

$$\boldsymbol{Co(NO_3)_2.6H_2O\ +2\,Fe(NO_3)_3.9(H_2O)+Gd(NO_3)_3.6H_2O\ +3.2\,C_6H_8O_7}$$

$$\boldsymbol{\rightarrow\ CoFe_{2-x}Gd_xO_4\ +42.8\,N_2\ +19.33\,CO_2\ +42.8\,H_2O}$$

3.4.1 Materials and Methods

Cobalt nitrate $[Co(NO_3)_2.6H_2O]$, Ferric nitrate $[Fe(NO_3)_3.9(H_2O)]$, Gadolinium nitrate $[Gd(NO_3)_3.6H_2O]$, and citric acid monohydrate as a chelating agent, Deionized Water (DI), dimethylformamide (DMF) and MWCNTs.

3.4.2 Synthesis of ferrites nanoparticles

Nanoparticles of $CoFe_{2-x}Gd_xO_4$ were synthesized by using the sol-gel method. The metal nitrate to citric acid molar ratio was determined to be $1:3$. Nitrate precursors were dissolved separately in de-ionized water in appropriate stoichiometric proportions for homogeneous mixing on the magnetic stirrer. After that, while stirring continuously, citric acid was added to the mixture as a complexing agent in an equal molar ratio to all of the metal nitrate precursors. Ammonia solution was used to alter the pH of the solution to 7. The resulting solution was then evaporated at $120℃$ until the transparent sol is obtained. The solution was then heated further while stirring until it became thick and a brown gel formed. Once the gel is formed, these were dried at about $250℃$ for the combustion of gel and converted into ash. The auto-combustion process known as a precursor produced the brown powder. Every final product that was created for this series was produced in a similar way. To produce the final product of nano crystalline $CoFe_{2-x}Gd_xO_4$ $(x = 0.0, 0.05, 0.10, 0.15,$ and $0.20)$ spinel ferrites, all of the samples powdered were sintered at $800\ °C$ for 4 hours.

3.4.3 Flow Chart

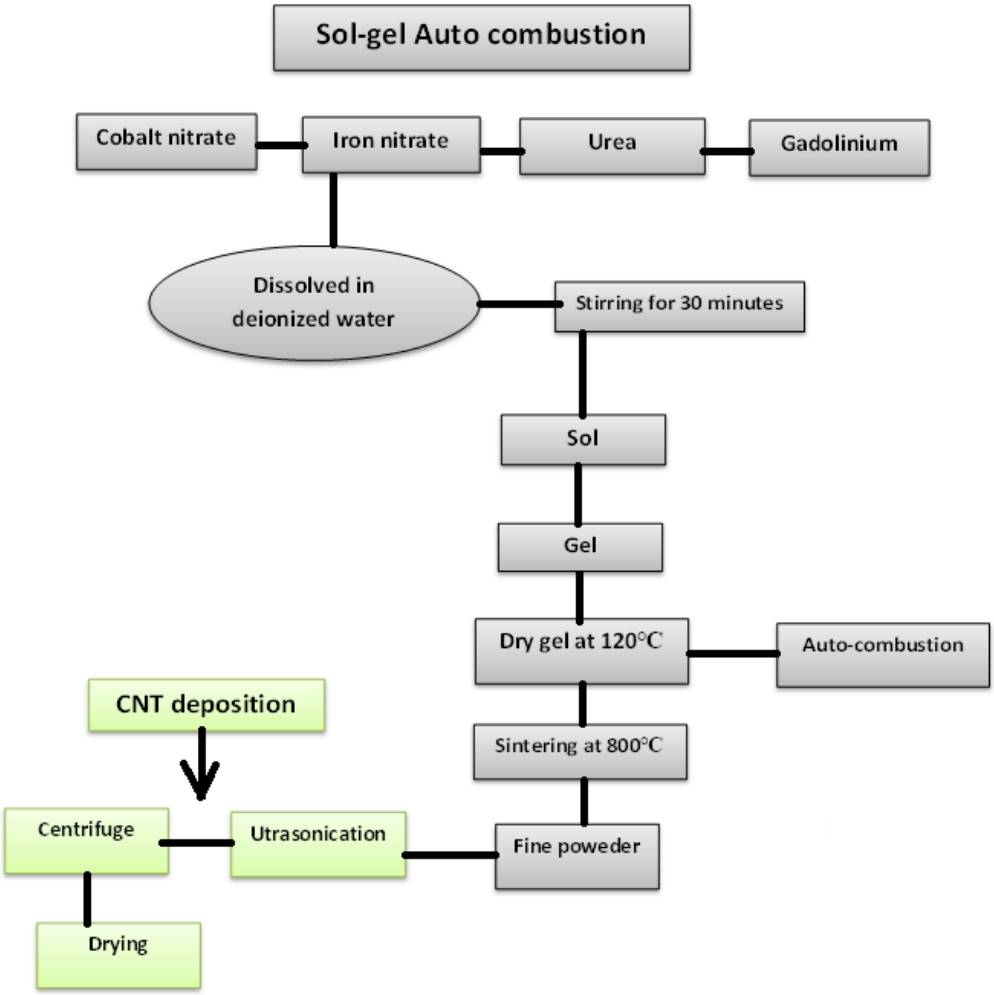

Fig 3.1: Flow chart of sol-gel method

3.4.4 Synthesis of composite materials

Chemically synthesized composite samples were created by inserting ferrite nanoparticles into a host $MWCNT$ with 1:1 weight ratio for $MWCNT$ - $CoFe_{2-x}Gd_xO_4$ samples. Firstly, $MWCNTs$ nanopowders were uniformly dispersed in the DMF solution through the ultrasonication method for 2 hours. Then, the ferrite nanoparticles were dissolved to the solution in appropriate weight ratio by magnetic stirring in the DMF solution. The resulting solution was then centrifuged

multiple times with deionized water and then dried and grinded to synthesized the final phase composite materials.

Fig 3.2: Schematic representation of CNTs deposition

3.5 Characterization Techniques

The properties of nanoparticles, such as their size, shape, and composition, are determined using various characterization techniques. Currently, there are several available methods for the characterization of NPs each driven by specific principles and mechanisms. To this end, energy dispersive X-ray analysis (EDX), Raman spectroscopy, scanning electron microscopy (SEM), photoluminescence spectroscopy (PL), ultraviolet–visible spectrometry (UV-visible), Fourier transform infrared (FTIR) operates on localized plasmon resonances and offers information about the morphology, elemental content and the optical characteristics of NPs are just a few of the techniques used [49]. Other techniques aimed at NPs characterization include dynamic light scattering (DLS), scanning tunneling microscopy (STM) and atomic force microscopy (AFM) for information about size, shape and surface characteristics and transmission electron microscopy (TEM) and X-ray photoelectron spectroscopy (XPS) providing information on size, shape and surface characteristics of the particles [49].

3.5.1 XRD (X-Ray Diffraction Analysis)

XRD analysis may be used for the identification of elements for the purpose of phase identification and for the qualitative and quantitative determination of their crystalline forms. The X-rays, as they interact with the atomic planes in a material, are transmitted, are diffracted, or absorbed. The X-rays that are diffracted form a pattern which is characteristic of the elements and spacing in the crystal. Crystallinity is the degree to which the atoms in a substance are spatially ordered. The greater the crystallinity, the sharper, more well-defined the XRD pattern, while the crystallography of an amorphous substance is reflected in a broad, diffuse pattern. The diffracted X-rays are proportional to the amount of the element contained in the material. XRD analysis is a powerful tool for materials characterization, with applications in many industries, including semiconductors, ceramics, pharmaceuticals, and more.

X-rays produce an X-ray tube by accelerating charged particles. This is the result of the application of a high voltage in two electrodes. Electrons are pushed towards the metal target, where, upon striking of their interactions with X-rays generate X-rays. X-rays are emitted in all directions. In XRD, the sample of crystalline material is hit with a beam of collimated X-rays. Some atoms in the crystal lattice scatter due to their interaction with X-rays. A detector at some distance picks up the scattered X-rays. The separation of atoms in a crystal lattice causes any X-rays that are scattered to do so at an angle. Bragg's law expressed as [50]:

$$2dsin\theta = n\lambda \tag{20}$$

Where:

- d is the distance between the atoms in the crystal lattice
- θ is the scattering angle
- n is an integer number
- λ represents the wavelength of the X-rays

Each crystalline material has its own unique pattern of scattered X-rays, which can be used to identify the material and deduce its crystal structure. In (X-ray diffraction) XRD, the X-ray source and detector opposite ends of a goniometer and the powdered sample is placed at the

center. Slits separate the X-ray source and the sample and more slits are places between the sample and the detector to both collimate the X-rays and reduce background noise. A sample holder interconnects with detector via the goniometer and allows the sample to rotate with respect to the detector at a 2:1 ratio. These setups assure that X-rays interact with the sample at all angles, generating a unique diffraction pattern for the material in question. Analysis of the material's diffracting pattern allows researchers to determine its crystal structure, among other characteristics [51].

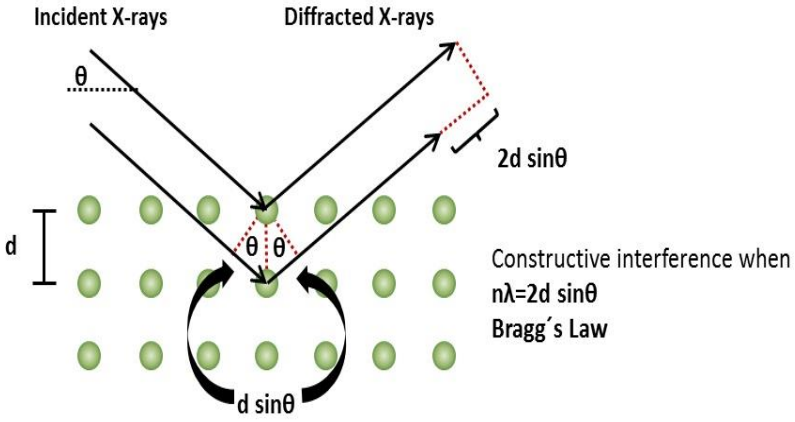

Fig 3.3: Schematic representation of Bragg's equation [52]

3.5.2 SEM (Scanning Electron Microscopy)

In both optical microscopy and scanning electron microscopy (SEM), a beam of energy is directed at a sample to form an image. However, the two techniques differ significantly in the type of energy used and the characteristics of the image produced. In optical microscopy, a beam of light is used to illuminate the sample. The sample interacts with the light, absorbing some of it, transmitting some of it and reflecting it. The reflected light is then captured by a lens, which focuses it down onto a detector. The light is transformed into an electrical signal by the detector, which is subsequently processed to produce an image. The primary limitation of optical microscopy is the wavelength of visible light, which is approximately 400-700 nm.

This means that optical microscopes cannot resolve features that are smaller than about 200 nm. In SEM an electron beam is used to illuminate the sample. Electrons in the sample interact with the atoms, either absorbing. The scattered electrons are then gathered by detector, which transformed into an electrical signal. The electrical signal is then processed to create an image. Since SEM isn't limited by the wavelength of light, like a traditional microscope, it can resolve features that are as small as a few nanometers making it an order of magnitude or two more powerful for imaging candid creatures. Optical microscopy is powerful technology for imaging microscopic objects, but it hasn't reached its limitations. It resolution is higher than that of SEM and has a larger depth of field, two areas where SEM falls short of the traditional tech. That said, combine the best bits of both systems and you'd have a technology that could image a much wider arrange of samples to a higher degree of detail.

The electron source, also known as electron cannon, is a crucial component of Scanning Electron Microscopy (SEM). There are two types of electron guns used in SEM to focus a high-energy electron beam, which is directed at the specimen. The field emission cannon focus electrons on the sample, immediately after they are released from atoms by a strong electric field. A thermionic gun, on the other hand, captures electrons by heating a filament. The ejected electron beam exposes the specimen surface to a variety of particles when using scanning electron microscopy; for instance, primary electrons, secondary electrons, Auger electrons, x-rays and so on. SEM employs primary, secondary, or backscattered electrons for image generation. Secondary electrons can be used to create high-resolution images in the 1 to 5 nanometer range. Additionally, backscattered electrons are employed for image creation, while characteristic x-rays are harnessed to analyze the elemental composition [53].

For raster scanning, the electron beam was concentrated by magnetic lenses after passing through the scanning coils and being deflected either horizontally or vertically over the sample's surface in a rectangular region. The signals are now tallied or detected, amplified with the aid of an electronic device or amplifier, and utilized to create an image on a cathode ray tube. The image displayed on the screen indicated the distribution [54].

The preparation of the sample is the stage that matters most in SEM. The SEM sample used should be conducted. When working with non-metals, a sputtering method must be used to

prepare them since non-metals need to be prepared because non-metals are poor conductors, have few free electrons, and quickly conduct electricity when blasted with electrons. A thin layer of a conducting substance, such as gold, is applied to make the non-metallic sample conduct [55].

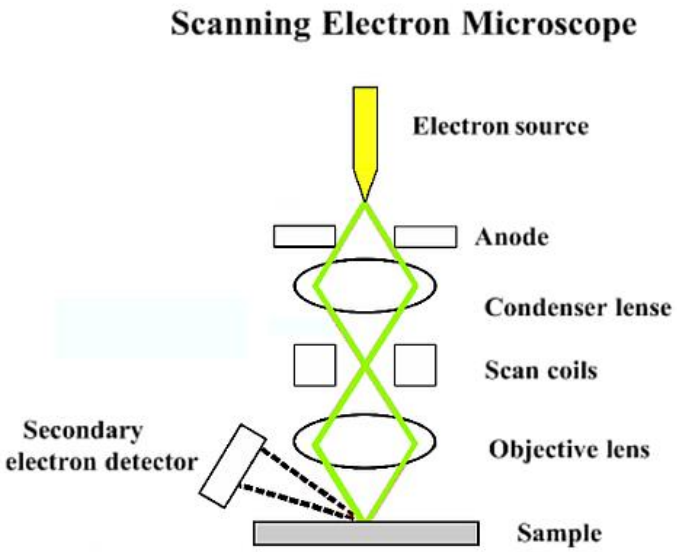

Fig 3.4: Diagrammatic illustration of a Scanning Electron Microscope [56]

3.5.3 EDX (Energy Dispersive X-ray Analysis)

In SEM the electrons ejected beam is focused on the specimen surface. X-rays, which are used to determine the composition of the specimen. The technique is called (EDX) analysis. EDX is used to get information about the element makeup of the near-surface region of the sample and to estimate the ratio of elements at various positions [57].

EDX (Energy-dispersive X-ray spectroscopy) is a commonly employed method that complements scanning electron microscopy (SEM) to recognize and measure the elements present in a sample. When conducting a scan using the EDX (Energy-dispersive X-ray spectroscopy) accessory, SEM (scanning electron microscopy) detects and measures elements present in a sample. In the EDX scan, the sample is bombarded with an intense electron beam, causing the atoms to emit X-rays. The energy of the X-rays is uniquely characteristic of the element from which they are emitted. The power of EDX analysis is its ability to enable one to discover the elemental composition of the material under study, particularly for heavy elements.

The weaknesses are that an EDX scan is not a surface examination, and it is an extremely slow procedure. The mix of the elements as well as the concentrations of nanoparticles at or near the surface can be calculated using EDX. Heavy metals like Ag, Au, and other such elements can easily be detected by EDX for their elemental makeup. EDX is unable to determine the elemental composition of light elements [58, 59].

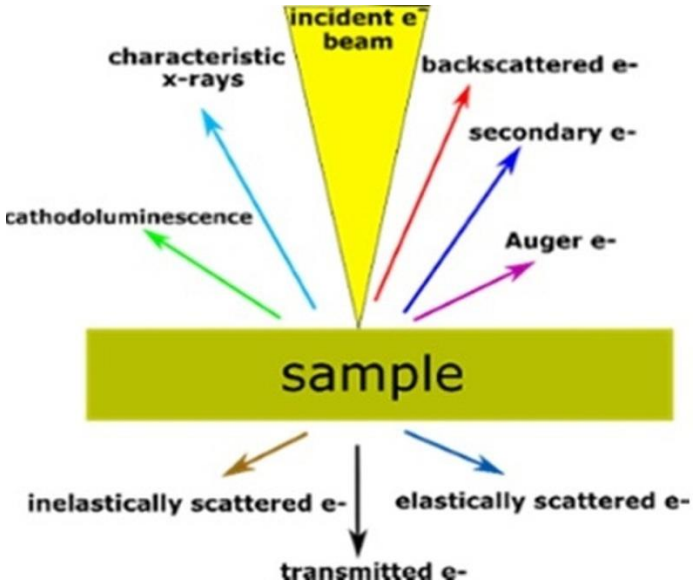

Fig 3.5: A Visual Guide to Energy-Dispersive X-Ray Analysis [60]

3.5.4 TEM (Transmission Electron Microscopy)

A high-magnification scanning technology named TEM records an electron beam passing through a material. The amplitude and phase shifts of the transmitted beam, which depend on the samples thickness (the amount of material the electron beam must pass through) and composition, produce imaging contrast. TEM imaging has significantly higher resolution than light-based imaging technologies because it illuminates the substance with electrons rather than light [61].

Achieving effective imaging of nanoparticles using TEM necessitates creating a distinct contrast between the sample and its background. In the preparation process for imaging, nanoparticles are dehydrated on a metal plate coated with a thin layer of carbon. The simplicity arises from the ease of capturing images of materials with electron densities significantly higher than that of amorphous carbon. This encompasses a range of materials, including most metals (gold, copper,

silver, and aluminum), common oxides (such as titanium, aluminum, and silica), and various particles like quantum dots, carbon nanotubes, magnetic nanoparticles, and polymer nanoparticles. TEM imaging stands out as the preferred method for directly assessing nanoparticle characteristics such as size distribution, grain boundaries, and shape. Typically, the size accuracy achieved is within a 3% margin of the actual values [62].

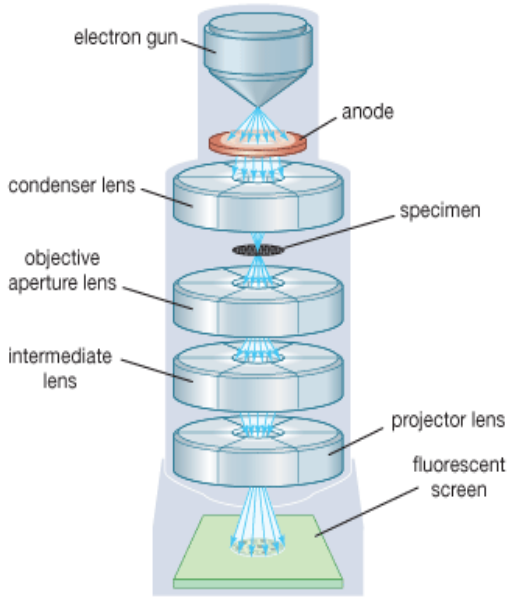

Fig 3.6: Schematic representation of Transmission Electron Microscopy [63]

3.5.5 FTIR (Fourier Transform Infrared Spectroscopy)

This method of spectroscopy utilizes IR light (infrared) to analyze samples and identify polymeric, inorganic, and organic compounds. Fourier-transform infrared spectroscopy (FTIR) scans the sample with infrared light and detects changes in absorption band patterns, indicating alterations in the composition of the specimen. It is valuable for identifying additives, assessing material decomposition or oxidation, detecting contaminants, and characterizing unidentified compounds.

In the FTIR process, the detector receives radiation from a source, which passes through an interferometer, gets amplified, and an A/D converter transforms it into a digital signal. The computer, where all FTIR procedures are executed, displays the amplified signal. The sample is exposed to infrared light with wavelengths ranging from $10{,}000\ to\ 100\ cm^{-1}$, and some of it is

absorbed while the rest is passed through the sample. The sample transforms the absorbed radiation into rotational or vibrational energy. The detector produces a signal with spectral range of $4000\ to\ 400\ cm^{-1}$ that represents the sample's molecular fingerprint. The uniqueness of each molecules imprint makes FTIR a valuable technique for compound identification [64, 65].

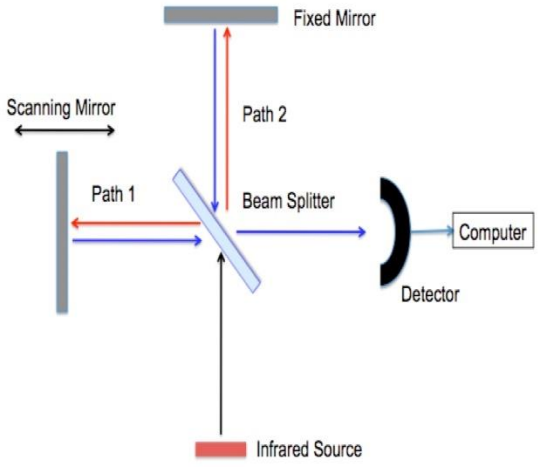

Fig 3.7: Principle of FTIR [66]

3.5.6 RAMAN (Raman Spectroscopy)

The characterization process involves utilizing the principles of inelastic scattering and Raman spectroscopy, employing laser light with a specific wavelength (monochromatic light) to analyze the vibrational, rotational, and other phases of a system. Raman scattering occurs as a result of interactions between phonon scattering and laser light in a system, causing an energy change that provides insights into the phonon modes. A monochromatic laser light is used to illuminate a specimen during Raman spectroscopy. The laser source emits electromagnetic (EM) radiation, striking a specific target or spot on the sample. The light is then collected by a lens and directed through a collimator. This process leads to the molecules of the specimen being elevated from their ground state to an excited state, known as Stokes-Rayleigh Scattering. Subsequently, the molecules are expected to relax from their excited vibrational mode or state. If the molecules are considered to be in an excited vibrational state, it is termed anti-Stokes Raman scattering.

Raman scattering occurs within the molecules, and the intensity of the scattering is contingent on the change in polarizability. The vibrational level forms the basis for the Raman shift [67, 68].

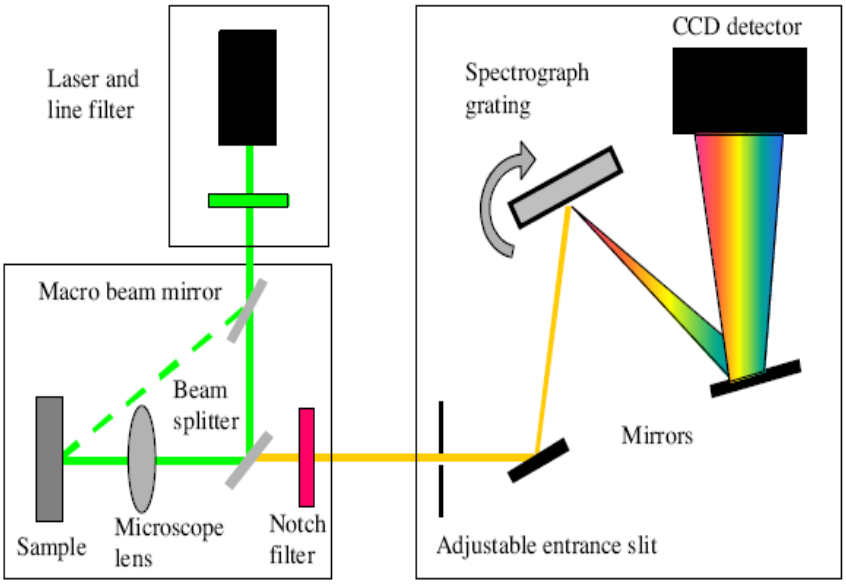

Fig 3.8: RAMAN Spectroscopy [69]

3.5.7 UV-Vis Spectroscopy

In UV-Vis spectroscopy, an ultraviolet lamp or Tungsten lamp serves as a source of ultraviolet or visible light, respectively. The setup includes additional components like a detector, monochromatic, sample unit, and reference beams. After exposure to UV radiation, the UV spectrum of the sample is determined. Cuvettes, which hold the sample and introduce it to the light channel, can be constructed from various materials such as glass, quartz, silica, plastic, or others. However, for studying absorbance below 310 nm, glass and plastic cuvettes are impractical. To assess the absorbance of the UV spectrum, quartz cuvettes are employed due to their transparency, allowing testing of absorbance for wavelengths beyond 180 nm [70].

3.5.7.1 Concept and Working

The reference beam is the light beam that reaches the detector without interacting with the sample, having traveled directly from the light source. When the sample is exposed to ultraviolet light characterized by continuously varying wavelengths resulting from the interaction of a sample beam with the specimen, electrons absorb radiation at specific wavelengths corresponding to their energy levels. This absorption propels the electrons to higher energy levels. The detector then gauges the disparity in intensity between the sample beam and the

reference beam. The wavelength is subsequently determined based on the maximum absorption exhibited by the sample [71]. A discrepancy in intensities becomes apparent when the reference strength surpasses that of the sample beam, indicating the specific wavelength with the highest UV absorption. This approach involves employing absorbance and reflectance spectra in the UV-visible part of the spectrum. As light traverses through the solution, some of its energy is absorbed, and the rest is transmitted. The ratio of the entering light to the light present in the specimen at a given wavelength is termed transmittance, with absorbance serving as the reciprocal of transmittance.

3.5.7.2 Beer-Lambert law

As per the well-established Beer-Lambert equation, the absorbance of a sample correlates directly with both its concentration and the path length at a specific wavelength. The Beer-Lambert equation is written as:

$$A = \varepsilon l c \tag{21}$$

Where:

- c represents concentration
- l denotes path length
- A stands for absorbance
- ε represents absorptivity

To avoid radiation scattering, it is essential for the medium to be homogeneous, and the incident light must possess a singular wavelength (monochromatic) [72].

Metallic nanoparticles, with a diameter of 100 nm, exhibit enhanced scattering of optical light due to surface plasmon resonance. This phenomenon occurs as the metallic conducting electrons collectively undergo plasmon resonance. The spectrum's bandwidth, wavelength, and the size of nanoparticles associated with plasmon resonance are all influenced by factors such as the surrounding environment, material composition, size, and shape [73].

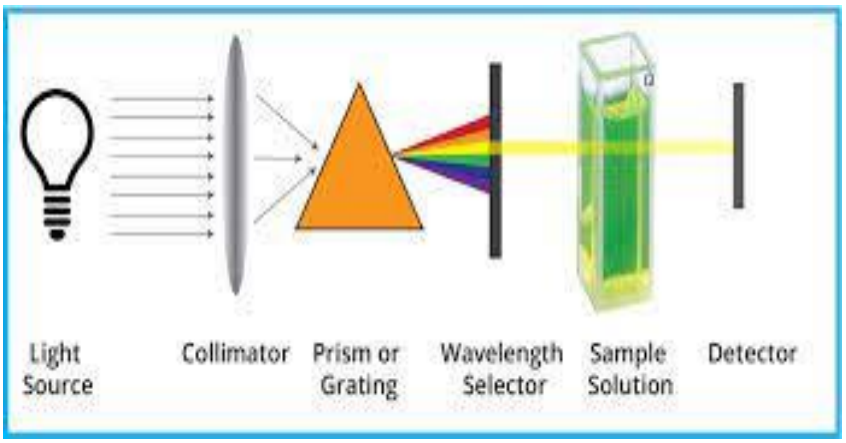

Fig 3.9: Schematic representation of Ultraviolet-Vis Spectroscopy [74]

3.5.8 Photoluminescence Spectroscopy (PL)

Photoluminescence, a form of luminescence resulting from photoexcitation, occurs when a substance emits light after absorbing photons from an external light source. Photoluminescence spectroscopy employs an optical spectrometer to assess the intensity of light emission across different wavelengths. It is recommended to excite all available electrons into an excited energy state using a high-intensity light source. Phenomena within photoluminescence can be categorized, with the recognition that samples include both radiative and non-radiative emissions. Photoluminescence is further divided into two main types of radiative emission: fluorescence and phosphorescence, each with distinct lifetimes due to differing energy transition routes. Calculating the photoluminescent quantum yield is a primary method for determining photoluminescence efficiency in a sample. Measurement tools such as the Ossila Optical spectrometer and a high-energy excitation source are required to characterize bulk material properties. Electrons are excited to higher energy levels by the excitation source, and the optical spectrometer detects the lower energy photons released as electrons relax [75].

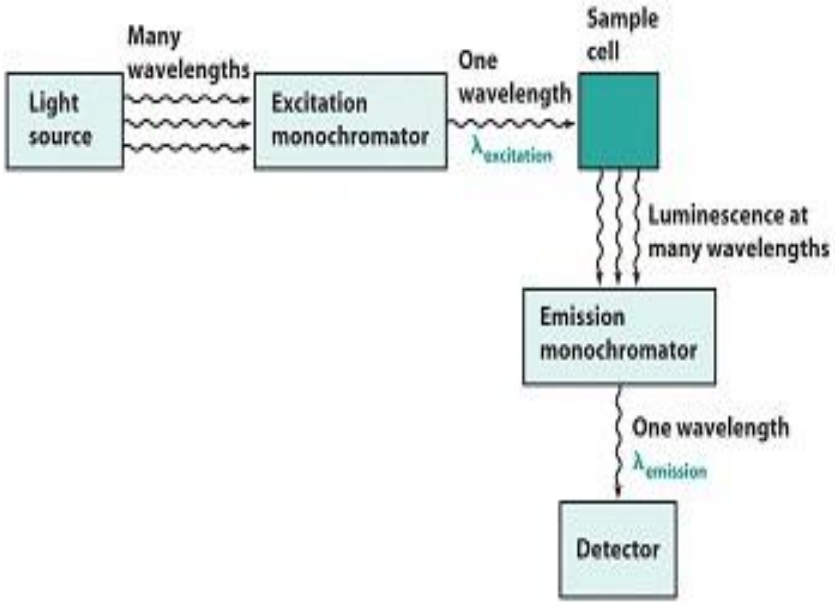

Fig 3.10: Schematic Representation of Photoluminescence Spectroscopy (PL) [75]

Chapter 4

Results and Discussion

4.1 UV-Vis Spectroscopy Results

The optical properties of as prepared cobalt ferrite nanoparticles are illustrated by UV-visible measurement in Fig 4.1. The figure shows the adsorption spectra from $190 - 800\ nm$ and Tauc Plot of prepared Gadolinium doped cobalt ferrites/$MWCNT$. The absorption spectra of all samples had a primary narrow weak and were found below $300\ nm$.

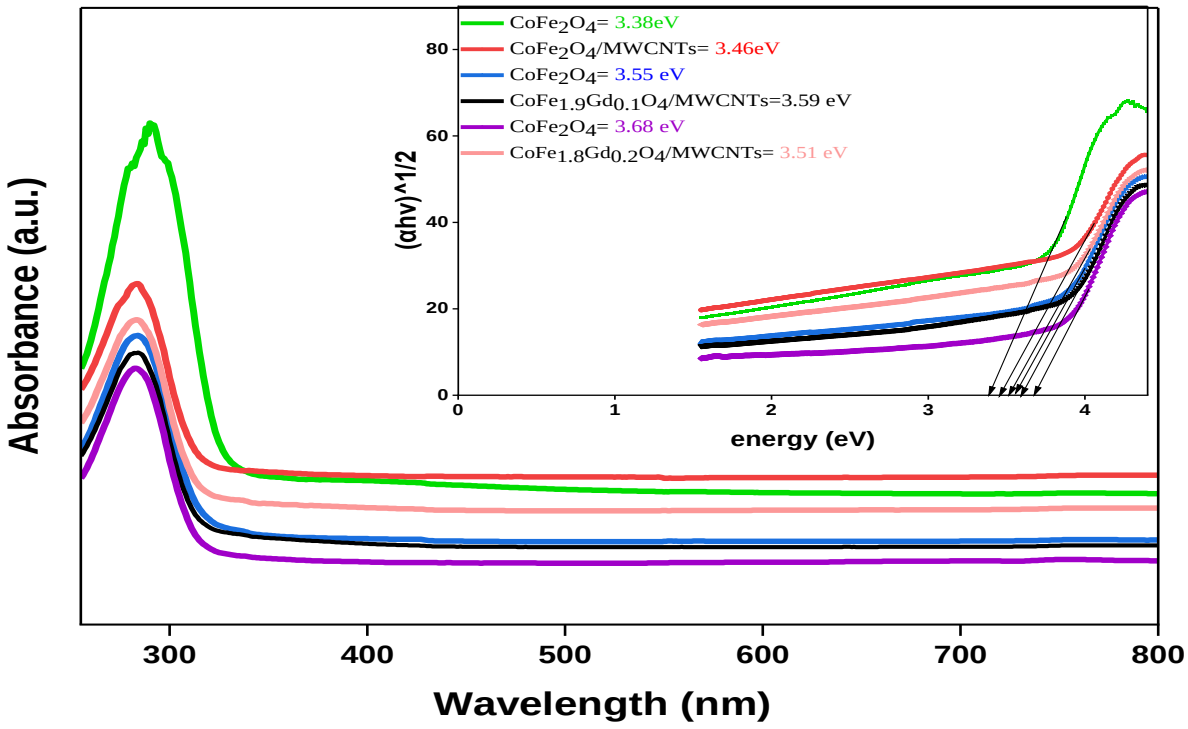

Fig 4.1: Absorbance spectra and Tauc Plot of Gadolinium doped cobalt ferrites.

The optical band gap energy (E_g) of the Gadolinium doped cobalt ferrites /$MWCNT$ samples has been calculated by using the Tauc's equation [75],

$$(\alpha h\nu)^{1/n} = A(h\nu - E_g) \tag{22}$$

Where:

- hv is the photon energy
- A is proportionality constant
- n is Tauc exponent

- E_g is an optical band gap of a semiconductor
- α is the absorption coefficient

A graph is plotted for $(\alpha h \nu)^{1/n}$ against the photon energy (eV). For $CoFe_{2-x}Gd_xO_4$ nanoparticles, the estimated band gap values are $3.32, 3.52$, and $3.69\ eV$ for $x = 0.0, 0.10$ and 0.20, respectively shows the increase in band gap with substitution. The CNT coating further improves the absorption properties. The band gap changes from 3.52 to $3.58\ eV$ for $x = 0.1$. The coating of CNT on all the samples resulted into increase in the band gap. The band gap values were estimated to be $3.42, 3.58$, and $3.60\ eV$ for Gadolinium doped cobalt ferrite–CNTs. It is well known that the band gap energy typically increases as the particle size decreases. This could be because the electron-hole pair gets extremely close when the crystallite size reaches the nanoscale, where all elements are composed of a finite number of atoms. As a result, the columbic force is not ignored for as long, which could lead to an overall increase in kinetic energy. A wider band gap, on the other hand, suggests that a significant amount of energy is required to excite one electron from the valence to the conduction band. At $x = 0.10$ concentration, crystallite size and band gap energy increased, most likely due to interfacial defects and the creation of energy levels [76]. A comparison of calculated band gap in this study is listed in Table. 4.1.

Table 4.1: Band gap of $CoFe_{2-x}Gd_xO_4$ and CNTs in DMF solution.

Composition	**Band gap (eV)**	**MWCNTs/ Band gap(eV)**
$CoFe_2O_4$	3.32 eV	3.42 eV
$CoFe_{1.90}\ Gd_{0.10}O_4$	3.52 eV	3.58 eV
$CoFe_{1.80}\ Gd_{0.20}O_4$	3.69 eV	3.60 eV

4.2 Fourier Transform Infrared Spectroscopy (FTIR)

FTIR spectra of the composites of cobalt ferrites and $MWCNTs$ in the range of $400-4000\ cm^{-1}$ were shown in fig 4.2. The functional groups that are referred as material signature are identified via IR spectroscopy. The spectra were examined for four samples including, $CoFe_{1.90}Gd_{0.10}O_4$ and $CoGd_{0.20}Fe_{1.80}O_4$ annealed at $800\ ^0C$ for 4 hours and CNT deposited samples. The FTIR

spectra of metal oxides confirm the existence of absorption bands within the 600– 1000 cm^{-1} range. The transmittance band is detected at around 626 cm^{-1} relates to *Fe–O* bond. The peak observes at 3604 $cm^{-1}$are assigned to OH stretching vibration of the free alcoholic group. The band at 3325 cm^{-1} is assigned to stretching vibrations of the *O–H* bond. Similarly, the bands associated with wavelengths 1694 cm^{-1} is appear due to carbonyl *C=O* stretch [77]. In $CoFe_{2-x}Gd_xO_4$, Fe^{3+} occupy both the octahedral and tetrahedral sites whereas Co^{2+} occupies the tetrahedral sites. Further, the wavelengths of 853 cm^{-1} and 626 cm^{-1} are associated with peaks that represent the *Fe–O* and *Co–O* stretching vibrations of the tetrahedral and octahedral sites, respectively [78].

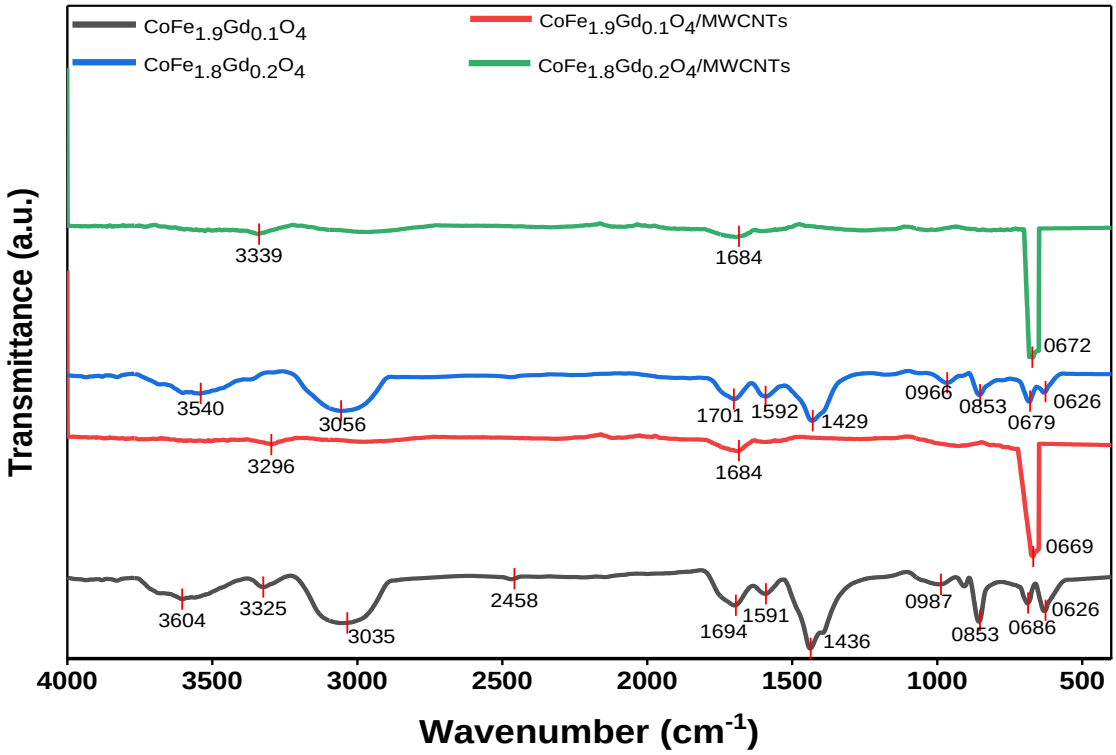

Fig 4.2: FTIR spectra of $CoFe_{2-x}Gd_x\ O_4$ nanoparticle and CNTs dispersed in DMF solution.

On the other hand, for the decorated CNTs, there is a broad absorption band with a small peak at 3296 cm^{-1} due to the stretching vibration of *O–H* and the peak at 1684 $cm^{-1}$is associated with the *C=O* stretching of the carboxylic acid ($-COOH$) group [79]. The peak at 669 $cm^{-1}$are

attributed to the $C-H$ bonds. The results show that decoration of the carbon nanotubes occurred, resulting in changes to the surface atoms and the nature of the functional groups.

4.3 SEM and EDX

Field emission scanning electron microscopy (FESEM) was used to analyze the morphologies of the ferrite nanoparticles. The results are shown in Figures 4.3(a), (b) and (c). The aggregation of the nanoparticles was observed as a result of the sintering. One or more of the adjacent nanoparticles facets serve as a link between the nanoparticles. Because of the high-temperature sintering process, nanoparticles have microstructure in shape. Utilizing a FESEM attachment, energy dispersive spectroscopy (EDS) was used to analyze the elemental compositions of the produced nanoparticles. As shown by Figure 4.3(c) typical EDS spectrum, the generated $CoFe_{2-x}Gd_x\,O_4$ ferrite nanoparticles are composed of *Co*, *Fe*, and *O* in nearly perfect stoichiometric composition, up to the EDS machine's detection limit.

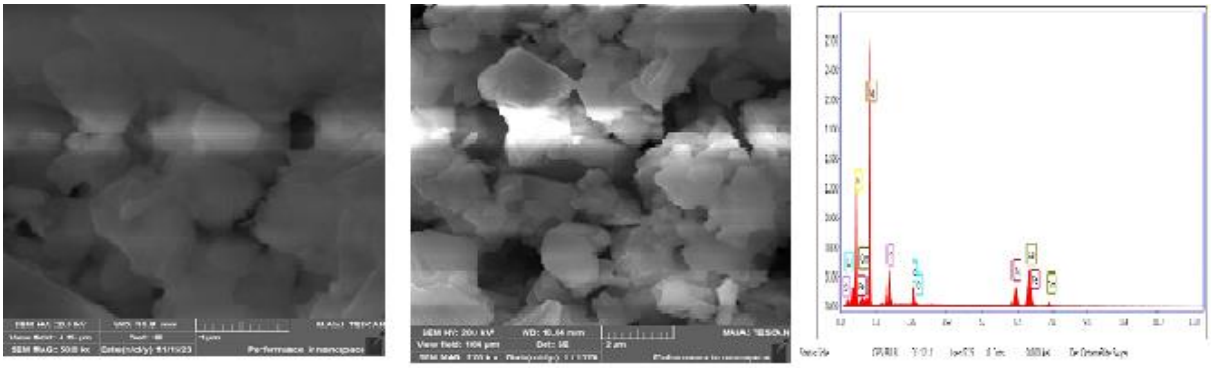

Fig 4.3: Typical (a) and (b) SEM images, and (c) EDX spectrum.

Ferrite nanoparticles were successfully placed in random configurations on the outer surfaces of $MWCNTs$ as seen by SEM micrographs of all composite samples in Fig 4.4. The $MWCNTs$ random dispersion in the composite samples is easily apparent, and their structure remains intact throughout any treatment. SEM images indicate that the surfaces of $MWCNTs$ are heavily contaminated with ferrite nanoparticles [80]. The chemical compositions of prepared samples are listed in table 4.2.

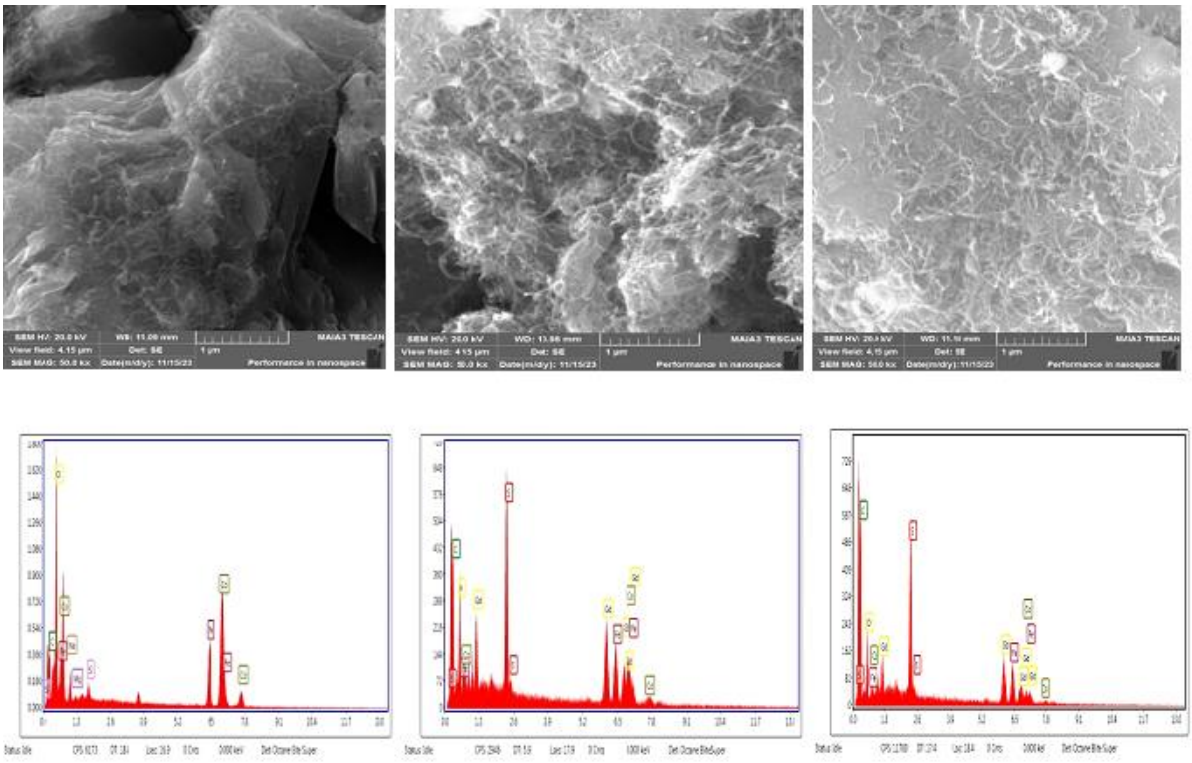

Fig 4.4: SEM images and EDX spectrum of $CoFe_{2-x}Gd_x\ O_4$ with deposited $MWCNTs$.

Table 4.2: Chemical composition of Samples via EDAX.

Sample	O		Fe		Co		Gd		C		Chemical formula
	Atomic% -Weight%										
1.	25.45	15.80	3.72	8.05	8.22	18.79	0	0	0	0	$CoFe_2O_4$
2.	34.66	24.59	5.66	14.01	11.94	31.21	0	0	38.59	20.55	
3.	27.19	16.98	8.38	18.28	2.00	4.59	0.61	3.73	0	0	$CoFe_{1.90}\ Gd_{0.10}O_4$
4.	14.21	10.08	3.54	8.76	3.41	8.90	3.78	26.37	68.41	6.43	
5.	30.97	13.12	8.18	12.10	4.80	7.49	9.12	37.97	0	0	$CoFe_{1.80}\ Gd_{0.20}O_4$
6.	13.45	12.34	2.10	6.71	0.67	2.28	1.90	17.16	77.46	3.37	

Conclusion

The nanocrystalline Gd-substituted cobalt ferrites have been prepared successfully by the technique of sol-gel auto-combustion. Gd doping has resulted as affected many properties of basic ferrites. Optical behavior of the ferrites has been observed band gap with varying energy $1-4\ eV$ which reveals the semiconducting tendency of the ferrites. Me-O bond and C-O bond are observed and the stretching of different bands are observed at different frequency. Doping effect is clearly evident of FTIR by movement to the higher frequency. Red shift is observed in the higher frequency region with the doping of Gd which is reported previously. And for the deposition of $MWCNTs$ enhanced further behavior of rare doped ferrite and by doping CNTs a change in the band is observed which is moving from 3.2 to 3.6 and presences of C-O is also observed in FTIR. SEM images indicated effective dispersion of MWCNTs with ferrite nanoparticles in the composite samples and showed a well-structured morphology. EDX spectroscopy confirmed the presence of Co, Gd, Fe, O and C in the investigated sample, verifying it's purity and the good reactivity at $800°C$.

References

[1] Kittel, C. (1955). *Solid state physics*. Shell Development Company.

[2] Ashcroft, N. W, & Mermin, N. D. (2022). *Solid state physics*. Cengage Learning.

[3] Wahab, M. A. (2005). *Solid state physics: structure and properties of materials*.

[4] Hofmann, P. (2022). *Solid state physics: an introduction*. John Wiley & Sons.

[5] Blakemore, J. S. (1985). *Solid state physics*. Cambridge university press.

[6] Grosso, G., & Parravicini, G. P. (2013). *Solid state physics*. Academic press.

[7] Kong, L.B., Liu, L., Yang, Z., Li, S., Zhang, T. and Wang, C., 2018. Theory of ferrimagnetism and ferrimagnetic metal oxides. In *Magnetic, Ferroelectric, and Multiferroic Metal Oxides* (pp. 287-311). Elsevier.

[8] HUTCHISON JR, C. A. (1955). Magnetic Susceptibilities. *Determination of Organic Structures by Physical Methods*, *1*, 259.

[9] Naseri, M. G., & Saion, E. B. (2012). Crystalization in spinel ferrite nanoparticles. *Advances in crystallization processes*, *14*.

[10] Omar, M. A. (1999). *Elementary solid state physics: principles and applications*. Pearson Education India.

[11] Pöttgen, R., Borrmann, H. and Kremer, R.K., 1996. Ferromagnetic ordering in CeAuGe. *Journal of magnetism and magnetic materials*, *152*(1-2), pp.196-200

[12] Puri, R. K., & Babbar, V. K. (2008). *Solid state physics and electronics*. S. Chand Publishing.

[13] Jain, V. K. (2022). *Solid State Physics*. Springer Nature.

[14] Mahmoud, R.S., El-Fadl, A.A., Abu-Sehly, A.A., Alotaibi, B.M., Alrowaily, A.W., Aboraia, A.M. and Shaaban, E.R., 2022. Structural, optical, and magnetic properties of iron-doped ZnO nanoparticles for optoelectronics. *Journal of Materials Science: Materials in Electronics*, *33*(30), pp.23484-23494.

[15] Goldman, A. (2012). *Handbook of modern ferromagnetic materials* (Vol. 505). Springer Science & Business Media.

[16] Pund, S.N., Nagwade, P.A., Nagawade, A.V., Thopate, S.R. and Bagade, A.V., 2022. Preparation techniques for zinc ferrites and their applications: A review. *Materials Today: Proceedings*, *60*, pp.2194-2208.

[17] Birajdar, A. A. (2023). *A Study of Initinal Permeability and Magnetic Properties of Ferrit Material*. Laxmi Book Publication.

[18] Gurav, S., 2023. *Investigation of MAGNETIC AND ELECTRICAL properties of some ferrite system prepared by chemical route*. Laxmi Book Publication.

[19] Hossain, M.D., Hossain, M.A. and Sikder, S.S., 2022. Hysteresis loop properties of rare earth doped spinel ferrites: A review. *Journal of Magnetism and Magnetic Materials*, p.170095.

[20] Malima, N.M., Khan, M.D., Choi, J., Gupta, R.K. and Revaprasadu, N., 2023. Alloying normal and inverse spinel (Zn–Co ferrite) nanostructures via direct precursor pyrolysis for enhanced supercapacitance and water splitting. *Materials Chemistry and Physics*, *302*, p.127770.

[21] Ejaz, S.R., Khan, M.A., Gulbadan, S., Akhtar, M.N., Ahmad, M., Hussain, A. and Islam, M.U., 2022. Structural, spectral, dielectric and magnetic properties of Co–Cr-substituted hexagonal ferrites with X-type structure. *Journal of the Korean Ceramic Society*, *59*(4), pp.453-464.

[22] Borhan, A.I., Ghercă, D., Iordan, A.R. and Palamaru, M.N., 2023. Classification and types of ferrites. *Ferrite Nanostructured Magnetic Materials*, pp.17-34.

[23] Verma, A. and Jasrotia, R., 2023. An Overview of Hard Ferrites: Types and Structures. *Materials Research Foundations*, *142*.

[24] Ball, P., 2005. Where is there wisdom to be found in ancient materials chemistry? *Chemistry International--Newsmagazine for IUPAC*, *27*(6), pp.13-16.

[25] Hu, B., He, M., Jakubowski, N., Meinhardt, J., Meyer, F.M., Niederstraßer, J., Schramm, R., Sindern, S., Stosch, H.G. and Bertau, M., 2017. *Handbook of Rare Earth Elements: Analytics*. Walter de Gruyter GmbH & Co KG.

[26] Henderson, P. ed., 2013. *Rare earth element geochemistry*. Elsevier.

[27] Atwood, D. A. (Ed.). (2013). *The rare earth elements: fundamentals and applications*. John Wiley & Sons.

[28] Almessiere, M.A., Korkmaz, A.D., Slimani, Y., Nawaz, M., Ali, S. and Baykal, A., 2019. Magneto-optical properties of rare earth metals substituted Co-Zn spinel nanoferrites. *Ceramics International*, *45*(3), pp.3449-3458.

[29] Zheng, B., Fan, J., Chen, B., Qin, X., Wang, J., Wang, F., Deng, R. and Liu, X., 2022. Rare-earth doping in nanostructured inorganic materials. *Chemical Reviews*, *122*(6), pp.5519-5603.

[30] Kannan, K., Radhika, D., Nesaraj, A.S., Sadasivuni, K.K., Reddy, K.R., Kasai, D. and Raghu, A.V., 2020. Photocatalytic, antibacterial and electrochemical properties of novel rare earth metal oxides-based nanohybrids. *Materials Science for Energy Technologies*, *3*, pp.853-861.

[31] Ismael, M., 2023. Environmental remediation and sustainable energy generation via photocatalytic technology using rare earth metals modified g-C3N4: A review. *Journal of Alloys and Compounds*, *931*, p.167469.

[32] Hossain, M.K., Khan, M.I. and El-Denglawey, A., 2021. A review on biomedical applications, prospects, and challenges of rare earth oxides. *Applied Materials Today*, *24*, p.101104.

[33] Ahmad, S., Ahmad, R. and Ahmad, I., 2019. Physical properties and possible applications of gold-based rare earth intermetallics (R-Au): A review. *Journal of Magnetism and Magnetic Materials*, *490*, p.165477.

[34] Nikmanesh, H., Jaberolansar, E., Kameli, P., Varzaneh, A.G., Mehrabi, M., Shamsodini, M., Rostami, M., Orue, I. and Chernenko, V., 2022. Structural features and temperature-dependent magnetic response of cobalt ferrite nanoparticle substituted with rare earth sm3+. *Journal of Magnetism and Magnetic Materials*, *543*, p.168664.

[35] Sarker, M.S.I., Yeasmin, M., Al-Mamun, M.A., Hoque, S.M. and Khan, M.K.R., 2022. Influence of Gd content on the structural, Raman spectroscopic and magnetic properties of $CoFe_2O_4$ nanoparticles synthesized by sol-gel route. *Ceramics International*, *48*(22), pp.33323-33331.

[36] Das, S.B., Singh, R.K., Kumar, V., Kumar, N., Singh, P. and Naik, N.K., 2022. Structural, magnetic, optical and ferroelectric properties of Y^{3+} substituted cobalt ferrite nanomaterials prepared by a cost-effective sol-gel route. *Materials Science in Semiconductor Processing*, *145*, p.106632.

[37] Rajeshwari, A., Punithavathy, I.K., Jeyakumar, S.J. and Jothibas, M., 2023. Dependance of gadolinium ions on structural, magnetic and dielectric properties of manganese nanoferrites. *Materials Chemistry and Physics*, *296*, p.127195.

[38] Khan, A.A., Khan, S.N. and Mir, A., 2022. Structural and electromagnetic characterization of yttrium doped copper ferrite. *Journal of Magnetism and Magnetic Materials*, *559*, p.169510.

[39] Bajaj, S., Andhare, D.D., Jadhav, S.A. and Shinde, S., 2023. Low temperature synthesis of in doped cobalt ferrite and investigations of structural, magnetic and dielectric properties. *Solid State Communications*, *360*, p.115016.

[40] Sarmah, S., Patra, K.P., Maji, P.K., Ravi, S. and Bora, T., 2023. A comparative study on the structural, magnetic and dielectric properties of magnesium substituted cobalt ferrites. *Ceramics International*, *49*(1), pp.1444-1463.

[41] Al-Juaid, A.A., 2023. La^{3+} substitution impact on structural, magnetic, and electrical properties of $CoFe_2O_4$ synthesized via sucrose auto-combustion. *Materials Research Express*, *10*(2), p.026101.

[42] Reddy, R.A., Rao, A.V., Babu, B.R., Rao, K.R. and Raghavendra, V., 2023. Structural, magnetic and antibacterial studies of gadolinium doped cobalt ferrite nanoparticles synthesized at low temperature. *Advances in Natural Sciences: Nanoscience and Nanotechnology*, *14*(1), p.015005.

[43] Jing, X., Guo, M., Li, Z., Qin, C., Chen, Z., Li, Z. and Gong, H., 2023. Study on structure and magnetic properties of rare Earth doped cobalt ferrite: the influence mechanism of different substitution positions. *Ceramics International*, *49*(9), pp.14046-14056.

[44] Rahardjo, D.T., Budiawanti, S., Suharno, S., Suryana, R., Supriyanto, A. and Purnama, B., 2023, May. Effect of yttrium doping on structural and magnetic properties in cobalt ferrite nanoparticles prepared by the sol-gel auto-combustion procedure. In *AIP Conference Proceedings* (Vol. 2604, No. 1). AIP Publishing.

[45] Rajput, N., 2015. Methods of preparation of nanoparticles-a review. *International Journal of Advances in Engineering & Technology*, *7*(6), p.1806.

[46] Hench, L.L. and West, J.K., 1990. The sol-gel process. *Chemical reviews*, *90*(1), pp.33-72.

[47] Mackenzie, J.D., 1988. Applications of the sol-gel process. *Journal of Non-Crystalline Solids*, *100*(1-3), pp.162-168.

[48] Sharma, V.K. and Marbaniang, D., 2019. Characterization Techniques of Nanoparticles Applied in Drug Delivery Systems. *Nanotechnology: Therapeutic, Nutraceutical, and Cosmetic Advances*, p.25.

[49] Nagasree, K.L.V., Suryanarayana, B., Raghavendra, V., Uppugalla, S., Mammo, T.W., Kavyasri, D., Murali, N., Raju, M.K., Parajuli, D. and Samatha, K., 2023. Influence of Mg^{2+} and Ce^{3+} substituted on synthesis, structural, morphological, electrical, and magnetic properties of Cobalt nano ferrites. *Inorganic Chemistry Communications*, *149*, p.110405.

[50] Ameen, F. and Majrashi, N., 2023. Recent trends in the use of cobalt ferrite nanoparticles as an antimicrobial agent for disability infections: A review. *Inorganic Chemistry Communications*, p.111187.

[51] Kamran, M., Abbas, Y. and Anis-ur-Rehman, M., 2023. Effect of Ce3+ and La3+ co-substitution on transport properties of spinel Co-Ferrites. *Inorganic Chemistry Communications*, *155*, p.111034.

[52] Noreen, S. and Hussain, A., 2023. Structural, optical, morphological and magnetic properties of Cu0. 25M0. 75Fe2O4 (M= Mn, Mg, Ni and co) ferrites for optoelectronic applications. *Optical Materials*, *139*, p.113797.

[53] Haque, A., Bhattacharya, S., Das, R., Hossain, A., Gayen, A., Kundu, A.K., Vasundhara, M. and Seikh, M.M., 2022. Effects of Bi doping on structural and magnetic properties of cobalt ferrite perovskite oxide LaCo0. 5Fe0. 5O3. *Ceramics International*, *48*(11), pp.16348-16356.

[54] Irshad, A., Zulfiqar, M., Ali, H.M., Shahzadi, N., Abd El-Gawad, H.H., Chokejaroenrat, C., Sakulthaew, C., Anjum, F. and Suleman, M., 2022. Co-substituted Mg–Zn spinel nanocrystalline ferrites: Synthesis, characterization and evaluation of catalytic degradation efficiency for colored and colorless compounds. *Ceramics International*, *48*(20), pp.29805-29815.

[55] Thakur, P., Gahlawat, N., Punia, P., Kharbanda, S., Ravelo, B. and Thakur, A., 2022. Cobalt nanoferrites: A review on synthesis, characterization, and applications. *Journal of Superconductivity and Novel Magnetism*, *35*(10), pp.2639-2669.

[56] Ristic, M., Krehula, S., Reissner, M., Jean, M., Hannoyer, B. and Musić, S., 2017. Synthesis and properties of precipitated cobalt ferrite nanoparticles. *Journal of Molecular Structure*, *1140*, pp.32-38.

[57] Hashim, M., Raghasudha, M., Meena, S.S., Shah, J., Shirsath, S.E., Kumar, S., Ravinder, D., Bhatt, P., Kumar, R. and Kotnala, R.K., 2018. Influence of rare earth ion doping (Ce and Dy) on electrical and magnetic properties of cobalt ferrites. *Journal of Magnetism and Magnetic Materials*, *449*, pp.319-327.

[58] Arshad, J.M., Raza, W., Amin, N., Nadeem, K., Arshad, M.I. and Khan, M.A., 2021. Synthesis and characterization of cobalt ferrites as MRI contrast agent. *Materials Today: Proceedings*, *47*, pp.S50-S54.

[59] Fakhari, S., Jamzad, M. and Kabiri Fard, H., 2019. Green synthesis of zinc oxide nanoparticles: a comparison. *Green chemistry letters and reviews*, *12*(1), pp.19-24.

[60] Susi, T., Meyer, J.C. and Kotakoski, J., 2019. Quantifying transmission electron microscopy irradiation effects using two-dimensional materials. *Nature Reviews Physics*, *1*(6), pp.397-405.

[61] Kwiecińska, B., Pusz, S. and Valentine, B.J., 2019. Application of electron microscopy TEM and SEM for analysis of coals, organic-rich shales and carbonaceous matter. *International Journal of Coal Geology*, *211*, p.103203.

[62] Kannan, M., 2018. Transmission electron microscope—Principle, components and applications. *A textbook on fundamentals and applications of nanotechnology*, pp.93-102.

[63] Mohamed, M.A., Jaafar, J., Ismail, A.F., Othman, M.H.D. and Rahman, M.A., 2017. Fourier transform infrared (FTIR) spectroscopy. In *Membrane characterization* (pp. 3-29). elsevier.

[64] Bacsik, Z., Mink, J. and Keresztury, G., 2004. FTIR spectroscopy of the atmosphere. I. Principles and methods. *Applied Spectroscopy Reviews*, *39*(3), pp.295-363.

[65] Guerrero-Pérez, M.O. and Patience, G.S., 2020. Experimental methods in chemical engineering: Fourier transform infrared spectroscopy—FTIR. *The Canadian Journal of Chemical Engineering*, *98*(1), pp.25-33.

[66] Dodo, K., Fujita, K. and Sodeoka, M., 2022. Raman spectroscopy for chemical biology research. *Journal of the American Chemical Society*, *144*(43), pp.19651-19667.

[67] Petersen, M., Yu, Z. and Lu, X., 2021. Application of Raman spectroscopic methods in food safety: A review. *Biosensors*, *11*(6), p.187.

[68] Smith, E. and Dent, G., 2019. *Modern Raman spectroscopy: a practical approach*. John Wiley & Sons.

[69] Weckhuysen, B.M., 2004. Ultraviolet-visible spectroscopy.

[70] Vitha, M.F., 2018. *Spectroscopy: Principles and instrumentation*. John Wiley & Sons.

[71] Shinde, G., Godage, R.K., Jadhav, R.S., Manoj, B. and Aniket, B., 2020. A Review on Advances in UV Spectroscopy. *Research Journal of Science and Technology*, *12*(1), pp.47-51.

[72] Mandru, A., Mane, J. and Mandapati, R., 2023. A Review on UV-visible spectroscopy. *Journal of Pharma Insights and Research*, *1*(2), pp.091-096.

[73] Akash, M.S.H., Rehman, K., Akash, M.S.H. and Rehman, K., 2020. Ultraviolet-visible (UV-VIS) spectroscopy. *Essentials of pharmaceutical analysis*, pp.29-56.

[74] Smith, E. and Dent, G., 2019. *Modern Raman spectroscopy: a practical approach*. John Wiley & Sons.

[75] Singh, T.A., Das, J. and Sil, P.C., 2020. Zinc oxide nanoparticles: A comprehensive review on its synthesis, anticancer and drug delivery applications as well as health risks. *Advances in colloid and interface science*, *286*, p.102317.

[76] Almessiere, M.A., Slimani, Y., Sertkol, M., Nawaz, M., Sadaqat, A., Baykal, A., Ercan, I. and Ozçelik, B., 2019. Effect of Nb3+ substitution on the structural, magnetic, and optical properties of Co0. 5Ni0. 5Fe2O4 nanoparticles. *Nanomaterials*, *9*(3), p.430.

[77] Anjum, S., Tufail, R., Rashid, K., Zia, R. and Riaz, S., 2017. Effect of cobalt doping on crystallinity, stability, magnetic and optical properties of magnetic iron oxide nano-particles. *Journal of Magnetism and Magnetic Materials*, *432*, pp.198-207.

[78] Rani, K. and Lekha, C., 2018. Green synthesis and characterization of silver nanoparticles using leaf and stem aqueous extract of Pauzolzia Bennettiana and their antioxidant activity. *Journal of Pharmacognosy and Phytochemistry*, *7*(5S), pp.129-132.

[79] Kuznetsova, A., Mawhinney, D.B., Naumenko, V., Yates Jr, J.T., Liu, J. and Smalley, R.E., 2000. Enhancement of adsorption inside of single-walled nanotubes: opening the entry ports. *Chemical Physics Letters*, *321*(3-4), pp.292-296.

[80] Sahoo, S., Sahoo, P.K., Manna, S. and Satpati, A.K., 2020. A novel low cost nonenzymatic hydrogen peroxide sensor based on CoFe2O4/CNTs nanocomposite modified electrode. *Journal of Electroanalytical Chemistry*, *876*, p.114504.